

Something about the structure of the Galaxy

Maartje N. Sevenster^{1,2}

¹*Sterrewacht Leiden, POBox 9513, 2300 RA Leiden, The Netherlands*

²*Presently at : RSAA/MSSSO, Private Bag Weston Creek PO, Weston 2611 ACT, Australia (msevenst@mso.anu.edu.au)*

Accepted xx. Received xx

ABSTRACT

We analyse a sample of 507 evolved (OH/IR) stars in the region ($10^\circ > \ell > -45^\circ$), ($|b| < 3^\circ$). We derive average ages for subsets of this sample and use those sets as beacons for the evolution of the Galaxy. In the Bulge the oldest OH/IR stars in the plane are 7.5 Gyr ($1.3 M_\odot$), in the Disk 2.7 Gyr ($2.3 M_\odot$). The vertical distribution of almost all AGB stars in the Disk is found to be nearly exponential, with scaleheight increasing from 100 pc for stars of $\lesssim 1$ Gyr to 500 pc for stars of $\gtrsim 5$ Gyr. There may be a small, disjunct population of OH/IR stars. The radial distribution of AGB stars is dictated by the metallicity gradient. Unequivocal morphological evidence is presented for the existence of a central Bar, but parameters can be constrained only for a given spatial-density model. Using a variety of indicators, we identify the radii of the inner ultra-harmonic (2.5 kpc) and corotation resonance (3.5 kpc). We show that the 3-kpc arm is likely to be an inner ring, as observed in other barred galaxies, by identifying a group of evolved stars that is connected to the 3-kpc HI filament. Also, using several observed features, we argue that an inner-Lindblad resonance exists, at ~ 1 –1.5 kpc. The compositions of OH/IR populations within 1 kpc from the galactic Centre give insight into the bar-driven evolution of the inner regions. We suggest that the Bar is ~ 8 Gyr old, relatively weak (SAB) and may be in a final stage of its existence.

Key words: Galaxy: structure – Galaxy: evolution – Galaxy: stellar content – Stars: AGB and post-AGB.

1 INTRODUCTION

It has become widely accepted that our Galaxy is barred, as evidence accumulated over the last five years from star counts, gas-dynamical studies and stellar three-dimensional kinematics and especially from the analysis of the COBE-DIRBE integrated-light data (Dwek et al. 1995; for a review on the galactic Bar see Gerhard 1996). The important parameters of a barred potential are the semi-major-axis length, a , the in-plane axis ratio, q , the pattern speed, Ω_p , and the strength relative to the axisymmetric part of the potential, A . From the observer’s point of view, another quantity is the major axis’ orientation with respect to the line of sight, the viewing angle ϕ . Due to the awkward view we have of the Galaxy, the values of those parameters are even harder to determine than in external galaxies. They are often inferred from the influence the barred potential has on the other parts of the galaxy. Helpful, albeit crude and not completely understood, diagnostics are the “resonant rings” and spiral features that arise at radii where orbits are in resonance with the frequency of rotation of the bar. The use of these structures is especially difficult in our Galaxy, where we see only tangent points to rings and spiral arms, but we

will attempt to do so.

The aim of this article is to describe the overall form of the stellar distribution in, and the evolution of various galactic components (disk, bulge, spiral arms etc), based mainly on its content of evolved stars and focussing mainly on the inner Galaxy. To a lesser extent, we attempt to constrain the free parameters of these stellar distributions. The goal is a schematic, rather than comprehensive, picture of the Galaxy.

We restrict ourselves largely to the stellar distribution and discuss the distribution of the gas only superficially. As stars are probably the source and the cleanest tracers of the barred potential, such a study of only the stellar component of the Galaxy is necessary. Obviously, the gas- and the stellar distributions should ultimately be explained simultaneously in one coherent picture. In fact, the first evidence for non-axisymmetry of the inner Galaxy came from the neutral-gas kinematics (see review by Oort 1977). It was exactly the drive for coherence that has shifted the attention to the stars, because their distribution showed no clear deviation from axisymmetry. Neither of the prevailing explanations for the origin of the observed radial gas motions - central expansion or elongation of the potential - were sup-

ported by stellar observations. Once the Bar had been found in the stellar surface density (Blitz & Spergel 1991; Dwek et al. 1995), questions remained. For instance, why are the stellar kinematics explained so well by axisymmetric models (Kent 1992; Ibata & Gilmore 1995) and why is the microlensing optical depth toward Baade’s window incompatible with density models derived from surface-density maps (eg. Nikolaev & Weinberg 1997) ?

The stellar data used in this paper (Sevenster et al. 1997a,b) were collected specifically to form the optimal sample to address such issues and to complement existing data. The sample consists of OH/IR stars: intermediate-mass, oxygen-rich, far-evolved asymptotic-giant-branch (AGB) stars. These are excellent tracers of the general stellar population, as stars with initial masses between roughly $1 M_{\odot}$ and $6 M_{\odot}$ go through this phase. They are also tracers of the galactic potential as they form a fairly relaxed population, with typical ages of several gigayears. Very strong and characteristic maser emission at 1612 MHz from the ground-state OH molecule allows for radio-interferometric observations, combining extinction-free coverage of the plane and fast sampling out to large distances with positions and velocities with negligible errors (compared to modelling errors). The employability of this sample in galactic-structure studies is clearly demonstrated in Sevenster et al. 1999.

The structure of this paper is as follows. In the first part, we discuss the large-scale spatial distribution of the OH/IR-star sample. We describe the sample of OH/IR stars in more detail in Sect.2. In Sect.3 we analyse the structure of this sample and estimate the scaleheights and -lengths for the galactic Bulge and galactic Disk. Variations of those exponential scales with position are combined with scales derived from similar samples and interpreted as age dependencies. In Sect.4, we give morphological evidence for a galactic Bar that cannot be explained by a physical lopsided distribution (see Blitz & Spergel 1991; Sevenster 1996). By comparing some parametrized models to the observations, a flavour of the values of the relevant parameters is obtained. Most importantly, we derive an approximate distance limit for the sample. The kinematic type of the galactic Bulge in terms of its anisotropy parameter and ellipticity is found.

In the second part of the paper we discuss the influence of the bar-shaped potential on the inner Galaxy. In Sect.5 we interpret various patterns found in the sample as resonant patterns and identify resonant radii. New insight into the nature of the so-called 3-kpc arm is provided by a small group of OH/IR stars that follows the 3-kpc arm’s longitude-latitude-velocity structure. In Sect.6 we give a description of the inner Galaxy based on the presented evidence and we speculate on its evolution in Sect.7. We conclude in Sect.8.

Throughout this article, we will use the term “Bulge” to denote the galactic component we see in the general direction of $|\ell| \lesssim 10^{\circ}$, without being interested in its actual form. If we use the term “Bar” we denote specifically the prolate or triaxial component of the Bulge. Unless explicitly stated otherwise, stellar velocities are given with respect to the local standard of rest (see Sevenster et al. 1997a,b for the used Doppler corrections) and $R_{\odot} \equiv 8$ kpc.

2 PROPERTIES OF THE DATA SET

The stellar density and the gravitational potential of the Galaxy are best traced by intermediate-mass, evolved stars as they constitute the largest fraction of the total stellar mass and are dynamically relaxed (Frogel 1988). Good candidates for this are the so-called OH/IR stars; oxygen-rich objects on the asymptotic giant branch (AGB; see for instance Habing 1993; Sevenster, Dejonghe & Habing 1995). We use an unbiased, homogeneous sample of 507 OH/IR stars in the galactic Plane, the AOSP sample (Australia telescope Ohir Survey of the Plane), acquired in a systematic survey of the region between longitudes $10^{\circ} > \ell > -45^{\circ}$ and latitudes $|b| < 3^{\circ}$ in the 1612 MHz (18 cm) OH-maser line (Sevenster et al. 1997a,b). The positional accuracy is $0''.5$, the line-of-sight velocities (with respect to the local standard of rest) are accurate to 1 km s^{-1} .

In Fig.1(a) we show the surface density of the AOSP sample, smoothed with an adaptive-kernel algorithm (Merritt & Tremblay 1994). With the initial kernel size that retains best the steepness of the central density profile without showing individual stars (1°) many local maxima are revealed in the distribution (R_{-1} , R_{-2} and R_{-3}). The maximum at $\ell = +9^{\circ}$ is likely to be a spurious edge effect. We will not discuss any asymmetries in the vertical direction, such as a tilt, because the data quality is slightly latitude-dependent (Sevenster et al. 1997a,b). First, in this section, we will assess some astrophysical properties of the sample.

The OH emission comes from an optically-thick, expanding circum-stellar envelope. Because the expansion is radiation-pressure driven, the unobservable intrinsic stellar luminosity L_{*} is related to the outflow velocity of the circum-stellar envelope, V_{exp} , and its gas-to-dust ratio, μ , (related to metal abundance Z ; $\mu \propto Z^{-1}$ for oxygen-rich stars, Habing, Tignon & Tielens 1994). According to van der Veen (1989):

$$L_{*} \propto \mu^2 V_{\text{exp}}^4. \quad (1)$$

This equation is derived and discussed in more detail in Appendix A. Separating the objects according to outflow velocity (Fig.1(b,c)) hence results in a separation roughly according to stellar luminosity, or age, without knowledge of the distances to the objects. This results, as expected, in very different apparent scaleheights of the subsamples (Fig.2, see discussion in Sect.3).

OH/IR stars can span a wide range of ages, of 0.1 Gyr to $\gtrsim 10$ Gyr. From the IRAS two-colour diagram, one can determine a “turn-over” [25]–[60] colour R_{32}^f , of sources leaving the evolutionary track (van der Veen & Habing 1988). This R_{32}^f is related to the initial mass (Garcia Lario 1991); this relation is discussed in Appendix B. We can thus find the initial mass of a star that has reached the end of the OH/IR-star phase (the thermally-pulsing AGB phase). Since this phase itself is short ($\sim 10^5$ yr, Tanabe et al. 1997) compared to the ages of the AGB stars, we can use the value for the AGB-tip ages by Bertelli et al. (1994) to obtain, for an assumed abundance, the age of the star from its initial mass. The minimum R_{32}^f for a sample hence gives the maximum age of the stars in that sample. We determined this for the Bulge region ($R_{32}^f > -0.4$, Sevenster et al. 1997a,b) and the Disk region ($R_{32}^f > +0.2$, Sevenster et al. 1997a,b) separately. We find minimum initial masses and

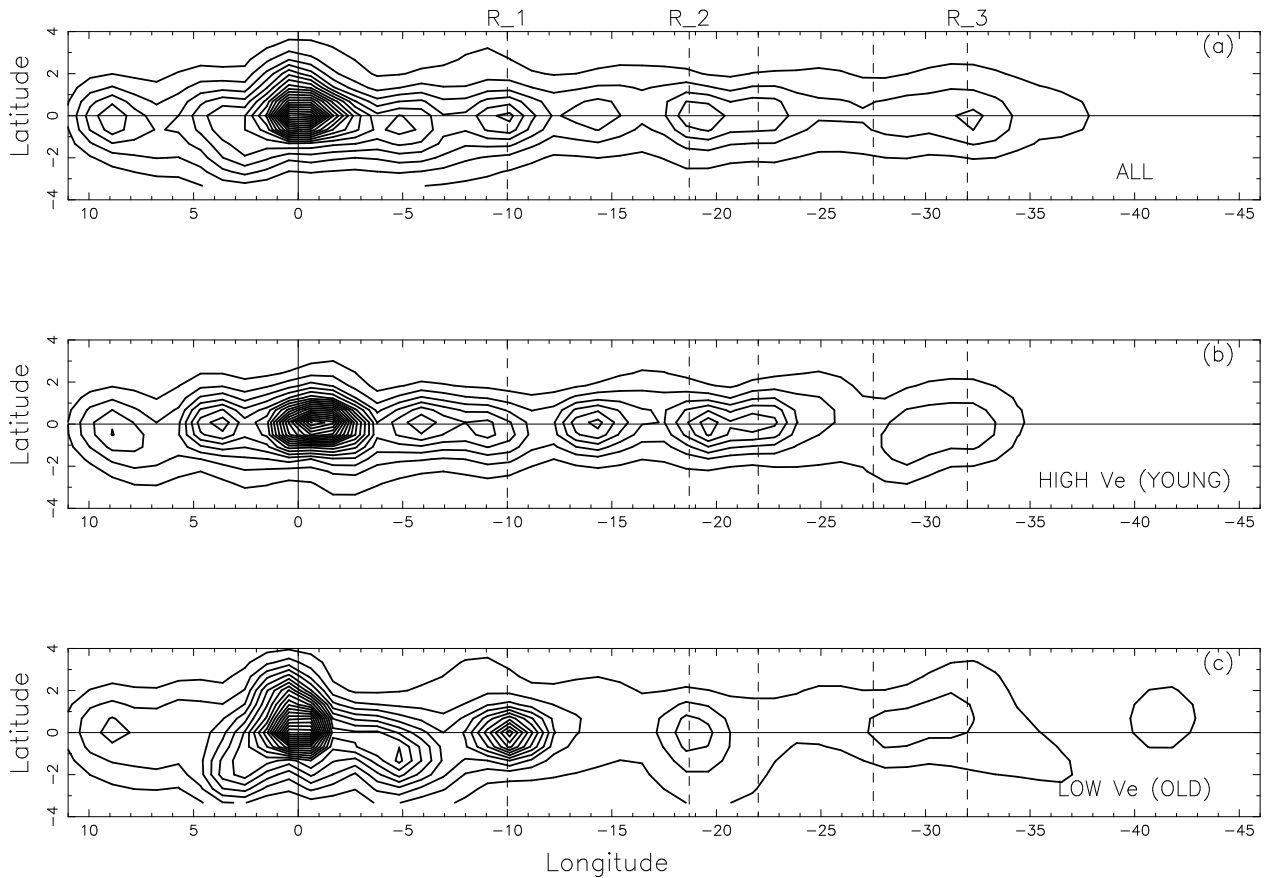


Figure 1 The surface density of the AOSP sample (Sect.2), in longitude versus latitude in degrees. The observations were smoothed with an adaptive-kernel algorithm (initial kernel of 1°). The upper panel is for all OH/IR stars (507), the middle for outflow velocities higher than 14 km s^{-1} and the lowest panel for outflow velocities lower than 14 km s^{-1} (and higher than 1 km s^{-1}). Panels **b**, **c** represent younger and older stars, respectively, with an abundance effect (Sect.2). Both subset-plots are based on ~ 210 stars. Note the offset toward negative longitudes in for the young sample (see Sect.4.1). The local maxima at $\sim -10^\circ$, -20° , -30° – R_{-1} , R_{-2} and R_{-3} , respectively – will be discussed in Sect.5. The unmarked vertical dashed lines indicate maxima in the observed 2.4 GHz distribution (see Sect.5, Fig.11). The maximum at $\ell = +10^\circ$ is not reliable. Contours are spaced at twenty even intervals between zero and the maximum of each particular plot.

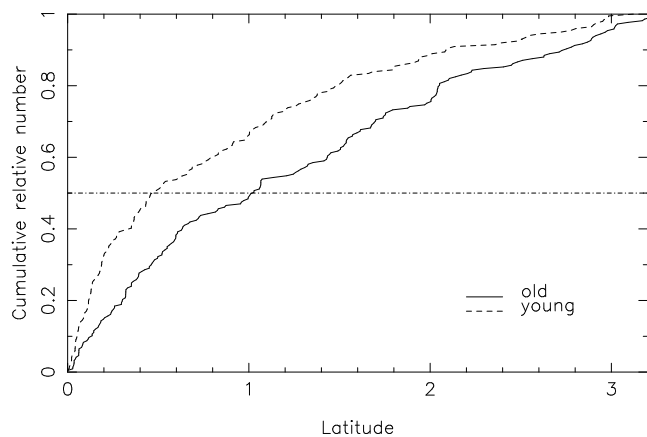


Figure 2 The cumulative-number distribution over latitude for the two subsamples of the AOSP sample (Fig.1(b,c)). The (apparent) scaleheights differ by a factor of 2, which is indicative of the age difference between the samples.

maximum ages of $1.3 M_\odot$ & 7.5 Gyr and $2.3 M_\odot$ & 2.7 Gyr , respectively, both for solar abundance. The ratio of the mean initial masses ($3.3/2.3$ with an $\text{IMF} \propto M^{-2.5}$, almost independently of Z used to derive the ages) and of mean outflow velocities ($15/14 \text{ km s}^{-1}$) are compatible with a similar average abundance for Disk and Bulge stars, $Z_b = 0.9-0.95Z_d$, according to equation (1). The number of stars in the AOSP sample with ages $\lesssim 0.5 \text{ Gyr}$ is negligible.

These values are meant to give an indication only, with a likely uncertainty of about 15% in the derived ages and about 10% in the initial masses. The $R_{32}^f - M_i$ relation is not yet fully established and should be used only for ensembles, not for individual objects. Besides, not all AOSP stars have a (reliable) IRAS identification (Sevenster et al. 1997a,b), although those that do must be representative of those that don't, as the identifications are hampered mainly by the confusion-limited spatial resolution of IRAS.

The ages are influenced by the fact that the AOSP sample covers only low latitudes. The fraction of (sub-) solar-mass OH/IR stars is apparently smaller than 1% at low latitudes. Out of the plane, van der Veen & Habing (1990) find the masses of oxygen-rich AGB stars to range to < 1.0

M_{\odot} , and the corresponding ages to well over 10 Gyr. However, with their mass-loss parameter $\epsilon_{\dot{M}} = 1.5$ instead of $\epsilon_{\dot{M}} = 1.0$ (both values are equally likely to be right), the mass range would be 1.2–2.2 M_{\odot} , which fits in very well with our derivations. Correspondingly, the ages of their stars would be lower, especially when using $Z = 0.02$ instead of $Z = 0.04$ as they advocate. We conclude that our results are compatible with theirs.

3 EXPONENTIAL SCALES OF THE DISK AND THE BULGE

The latitude distribution of the AOSP sample is steeper than a (projected) exponential ($\exp(-z)$) at all longitudes and irreconcilable with flatter functional forms ($\text{sech}^2(z)$ or $\exp(-z^2)$). The same was found recently by de Grijs & Peletier (1997) for a large number of spiral galaxies; Kent, Dame & Fazio (1991) found from NIR observations of the Galaxy that the profile is closer to exponential than to $\text{sech}^2(z)$. To obtain estimates of the values of the scalelength and scaleheight of the spatial density, we hence used double exponentials ($\rho \propto \exp(-R/h_R) \exp(-z/h_z)$). We estimated those values in various regions of the sky, to assess variations of the scales with radius and height (age). Note, however, that we are not trying to model the Galaxy as a set of double exponentials.

We fitted cumulative-number densities with single exponentials, in latitude (in $R_{\odot} \tan b$); $R_{\odot} \equiv 8$ kpc) and longitude (in $R_{\odot} \sin \ell$) separately. This yielded apparent scales h_{zb} and $h_{R\ell}$ of the local surface-density distribution at various longitudes and latitudes (Fig.3). Due to the non-trivial angles between lines of sight, the scales are not invariant for projection, even though the Galaxy is seen edge-on. This means we have to deproject the apparent scales to find the true scales h_z and h_R . By projecting analytic double-exponential distributions with a range of h_R and h_z , we obtained a range of apparent scales at the same (ℓ, b) as the data measurements. We could thus retrieve the intrinsic (h_z, h_R) that would yield a measured pair $(h_{zb}, h_{R\ell})$. Projection effects cause the relation between the true and the apparent scales to depend upon longitude and latitude, and also upon each other, thus jeopardizing a unique deprojection.

However, for all our measurements, except those at C (Fig.3), this technique gave unique results (Table 1, columns 3–6), within the context of using double exponentials. In Table 1 the deprojected scales are also given for the high- and low-outflow sources separately, determined over the whole latitude range of the survey. For the galactic disk ($|\ell| \lesssim 15^\circ$), most references (see Sackett 1997) give $h_R = 2.5$ –4.5 kpc and $h_z = 250$ –400 pc (“thin”) and $h_z = 750$ –1500 pc (“thick” disk).

3.1 Ring ?

The very large apparent scalelength at $\ell \sim -18^\circ$ (C; Fig.3) indicates a flat distribution in longitude. With this value of the measurement, the deprojection is not unique. Nevertheless, our tests showed that projection effects alone, although being largest at these longitudes, can not explain the extreme apparent scalelength and we conclude it is intrinsic. The flat distribution is formed mainly by the high-outflow (and single-peaked) sources, ie. the younger stars (Table 1,

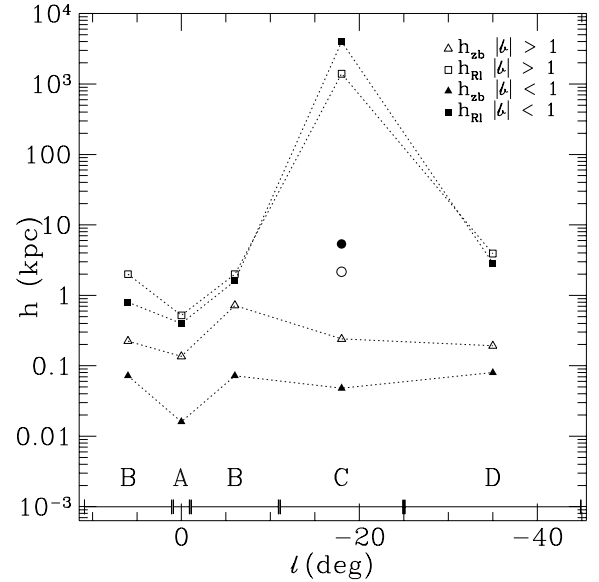


Figure 3 The local apparent exponential scaleheights h_{zb} and $h_{R\ell}$ of the AOSP sample, from fits to the cumulative distributions in latitude and longitude separately. The symbols are for $0 < |b| < 1$ (closed) and $1 < |b| < 3$ (open), respectively. The bars along the abscissa indicate the longitude bins (A,B,C,D) used for the determination of the fits; the data points are at the middle values of these bins. All longitude bins contain about 100 stars over the full latitude range ($|b| < 3^\circ$); the formal errors on the measurements are $\sim 15\%$. The two circles are the scalelengths fitted to low-outflow stars (cf. Fig.1(c)) only. For A the apparent scaleheight is very small due to the presence of the galactic-centre population (see Sect.3.2). Very large apparent scalelengths, such as in longitude bin C, are equivalent to an infinite scalelength or a (locally) flat distribution (Sect.3.1).

column 7 vs. 9; Fig.3(circles)). This region around $\ell = -18^\circ$ will be treated in more detail in Sect.5, where we find that the distribution in that direction is probably dominated by a ring structure.

3.2 Central disk

A deciparsec-scale, flat, rapidly-rotating flat population of OH/IR stars is present in the galactic Centre (Lindqvist, Habing & Winnberg 1992; Sevenster et al. 1995). Even though the AOSP sample contains only 19 out of the 134 known OH/IR stars in this region (Lindqvist et al. 1992; 52 more were discovered by Sjouwerman et al. 1998a), we can still resolve its very low scaleheight with respect to other regions (Table 1, column 5). As was known before, the central disk is seen primarily in the high-outflow sources (Table 1, column 10).

However, the scalelength of 250 pc (Table 1, column 3) is unlikely to represent this small central disk. Indeed, if we apply our method to the full sample of Lindqvist et al. (1992) we find $h_z = 20$ pc and $h_R = 40$ pc, the same values as they find themselves (Table 1, columns 3,5 between brackets).

3.3 Outer Galaxy

Hardly any OH/IR stars are known outside the solar circle. Carbon-rich AGB stars, on the other hand, are hardly

Table 1. Deprojected exponential scales for the squares and triangles in Fig.3 (columns 3–6) and for low- (“o”, columns 7,8) and high-outflow (“y”, columns 9,10) sources ($|b| < 3^\circ$). The values between brackets are from another sample at $|\ell| = 0^\circ$ (see text) or conceivably unreliable because of the infinite value of h_R at $|\ell| = 18^\circ$.

	$ \ell $ $^\circ$	$h_R(b < 1^\circ)$ kpc	$h_R(1^\circ < b < 3^\circ)$ kpc	$h_z(b < 1^\circ)$ pc	$h_z(1^\circ < b < 3^\circ)$ pc	$\overline{h_R(o)}$ kpc	$\overline{h_z(o)}$ pc	$\overline{h_R(y)}$ kpc	$\overline{h_z(y)}$ pc
A	0	0.25(0.04)	0.25	10(20)	150	0.2	200	0.35	30
B	6	0.95	0.75	90	350	0.75	250	0.75	100
C	18	∞	∞	(100)	(300)	10.0	350	∞	(10)
D	35	3.5	5.5	100	250	10.0	200	1.5	100

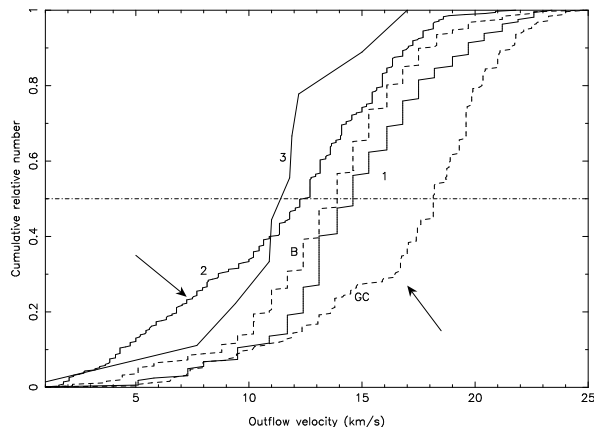


Figure 4 The cumulative-number distributions of outflow velocities for double-peaked OH/IR stars from various samples: 1. Disk AOSP sample; 2. Arecibo sample (Chengalur et al. 1993); 3. Outer Galaxy (Blommaert et al. 1993); B. Bulge AOSP sample; GC. galactic-centre sample (Sjouwerman et al. 1998a). The median outflow velocity correlates with metallicity (equation (1)); its decrease with larger mean radius (in order : (GC,B) 1,2,3) reflects mainly the galactic metallicity gradient. The small difference between “1” and “B” is mainly due to a mean-mass difference, however. The arrows indicate deviant sub-populations of distribution “2” (thick disk; discussed in Sect.3.4) and “GC” (star burst; Sect.7). Except sample “3” that consists of 9 stars, all samples contain more than 200 stars.

seen in the inner Galaxy (see the figures in Blanco 1965). Blommaert, van der Veen & Habing (1993) find that the few OH/IR stars in the outer Galaxy have initial masses of at least 2–3 M_\odot , similar to the AOSP disk stars (Sect.2). The low outflow velocities of the sample (the median is 3 km/s lower than for the Disk AOSP sample, Fig.4) indicate low metallicity (equation (1)), as was observed by Blommaert et al. (1993). At intermediate longitudes ($\ell \sim 50^\circ$), the OH/IR stars from the Arecibo survey (Chengalur et al. 1993) have initial masses and ages similar to the Bulge AOSP sample (Sect.2) and slightly lower median outflow velocity.

The decrease in outflow velocities with higher longitude is the result of decreasing metallicity. The galactic-disk metallicity gradient ($-0.07 \text{ dex kpc}^{-1}$ from oxygen, Smartt & Rolleston 1997) corresponds, for constant mass, to an outflow-velocity gradient of $\sim 1 \text{ km s}^{-1} \text{ kpc}^{-1}$ (for $V_{\text{exp}} \sim 14 \text{ km s}^{-1}$, equation (1)).

At the same time, at lower metallicity, the limiting mass above which stars remain oxygen-rich and below which carbon-rich stars form increases. The upper limit to the

mass for which a star will reach the AGB in turn becomes lower with lower abundance (see Bertelli et al. 1994). The upper limit to the outflow velocities will decrease even more noticeably (equation (1)); this explains the small scalelength for the high-outflow sources (Table 1). The abundance may decrease rather suddenly around $R = 6 \text{ kpc}$, as observed by Simpson et al. (1995). They explain this by assuming this is the outer edge of the zone-of-influence of the Bar. As we will see later (Sect.6), the Bar’s outer-Lindblad resonance (OLR, Binney & Tremaine 1987 (BT) Ch.6) may indeed have a radius of 6–7 kpc.

3.4 The Arecibo sample

With respect to an otherwise equivalent sample (te Lintel et al. 1991), the Arecibo sample has twice as many sources at outflow velocities $\lesssim 9 \text{ km s}^{-1}$ (Fig.4, see left-most arrow). This difference is significant to 99.8% (Kolmogorov-Smirnov). The apparent scales of the subset with outflow velocities $< 10 \text{ km s}^{-1}$ (Fig.6) are $h_{zb} = 1.1 \text{ kpc}$ and $h_{R\ell} \rightarrow \infty$ (Fig.5). Again, the nearly-infinite apparent scale-length makes unique deprojection impossible, but we found that the apparent scaleheight is most probably close to the true scaleheight in this case. These stars might be part of the 1-kpc thick disk claimed by other authors (Habing 1988; Gilmore & Reid 1983, Ojha et al. 1996), although Blommaert et al. (1993) conclude that true AGB stars do not partake in the thick disk and there is no sign of this population in the te Lintel (et al. 1991) sample. In Fig.6, we see that these low-outflow stars are not concentrated toward the plane. This may be a selection effect as the Arecibo sample was acquired in a detection experiment toward IRAS-selected point sources, but this is also true for the te Lintel (et al. 1991) sample. Moreover, when we select stars from the Arecibo sample in the same latitude range as the AOSP sample a small excess is still present (Fig.7).

So, in the Arecibo sample we see an extra population with low outflow velocities and a gap in the latitude distribution. The latter brings to mind the intriguing “levitation” process (Sridhar & Touna 1996a,b), a vertical-to-radial resonance. This would not explain an excess of sources, however. If the excess sources have low metallicity, rather than only low masses (equation (1)), this population could have been accreted anytime during the last 10 Gyr from a dwarf such as Fornax ($[\text{Fe}/\text{H}] < -0.7$). With the observational limit of less than five such more metal-rich dwarfs accreted in the last 10 Gyr (Unavane, Wyse & Gilmore 1996) this is a possibility.

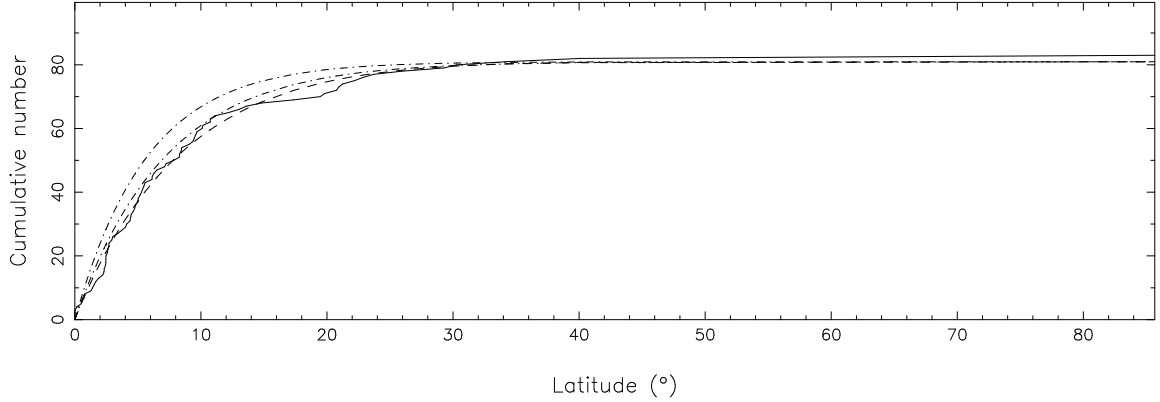


Figure 5 The cumulative–latitude distribution of all Arecibo stars with outflow velocity $< 10 \text{ km s}^{-1}$ (solid, cf. Fig.4, 6). The fit (dashed) is a projected double–exponential distribution with apparent scaleheight $h_{zb} = 1.1 \text{ kpc}$. For comparison, the dot–dashed lines give the distribution for $h_{zb} = 800 \text{ pc}$ and 1 kpc , respectively. The intrinsic scaleheight is probably close to 1.1 kpc as well.

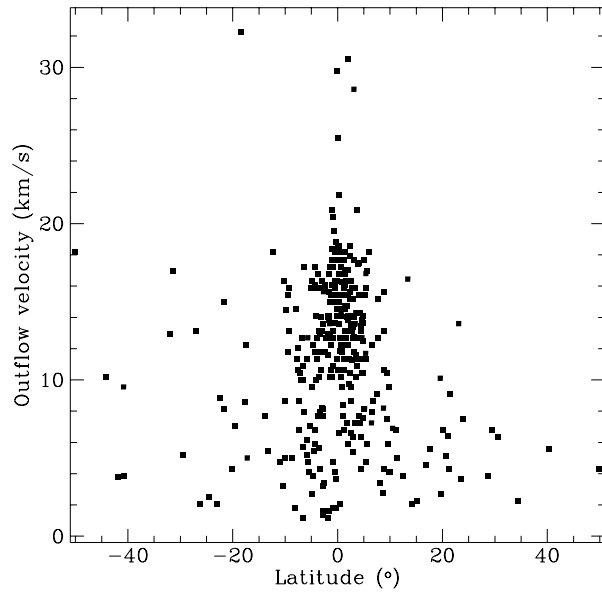


Figure 6 The distribution of the Arecibo stars over latitude and outflow velocity. There is a difference in the concentration toward the plane at low latitudes between stars with outflow velocities higher and lower than 10 km s^{-1} , respectively. Below 10 km s^{-1} there is also a clear excess of sources (50%) in the Arecibo sample with respect to the other samples in Fig.4. These stars form possibly a thick disk.

3.5 Radial and vertical variations

Clearly, one double–exponential cannot describe the distribution of OH/IR stars. The older disk stars (few Gyr) seem to trace an exponential disk with rather large scalelength plus a central component with similar vertical scale (Table 1). The younger stars ($< 1 \text{ Gyr}$) follow a more capricious pattern and have varying, but small vertical scales. This is not unexpected since they have completed only a few rotations

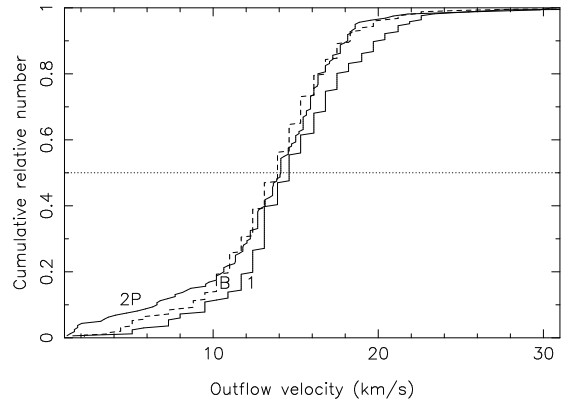


Figure 7 As Fig.4, for the Bulge AOSP sample (“B”, 250 stars in the plot), the Disk AOSP sample (“1”, 165 stars) and the stars of the Arecibo sample with $|b| < 3^\circ$ (“2P”, 160 stars). There is still an excess of sources below $V_{\text{exp}} = 10 \text{ km s}^{-1}$ for “2P”. Note that the distribution of higher outflow velocities of “2P” is much more like “B” than like “1”.

around the galactic Centre since their formation and therefore phase mixing, let alone radial mixing, has not yet been effective. There seem to be no sudden transitions in the distribution; except that from the flat distribution ($h_R \rightarrow \infty$) to the outer disk ($h_R = 1.5 \text{ kpc}$) for the high–outflow sources that is rather abrupt. As we will see later (Sect.5), this may be around the radius of corotation with the pattern speed of the central Bar. The radial scale derived (via the same procedure described earlier) from the Arecibo sample (using only $|b| > 8^\circ$ because of its incompleteness in the plane) and from a sample of carbon–rich AGB stars ($|\ell| \sim 60^\circ$, $|b| < 15^\circ$, Loup et al. 1993), is $\sim 10 \text{ kpc}$; the same as from the low–outflow OH/IR stars. So, except for the massive oxygen–rich objects, the scalelength is found to be similar for all AGB stars. The very different radial distributions of C–rich and O–rich AGB stars, respectively, is governed by the metallicity gradient only.

Outside the AOSP-survey window, we also derived scaleheights from the Arecibo subsample and the Loup sample, and found $h_z \sim 500$ pc for both. The full sample of outer-Galaxy AGB (not only OH/IR) stars of Blommaert et al. (1993) has $h_z \lesssim 400$ pc. The vertical scale appears to increase with latitude from ~ 100 pc to ~ 500 pc, irrespective of the longitude range. The increase in scaleheight within the Disk AOSP sample agrees with the diffusion models by Wielen (1977) for age increasing from $\lesssim 1$ Gyr to $\gtrsim 2$ Gyr. The scaleheight of 500 pc for the oldest AGB stars is the same as that for white dwarfs as given in Mihalas & Binney (1981).

3.6 In short

In summary, the AGB stars are distributed in the thin (old) disk with a scaleheight of 100 pc for the youngest AGB stars ($\lesssim 1$ Gyr). The scaleheight increases continuously to 500 pc for AGB of $\gtrsim 5$ Gyr. The scaleheights for the Disk and the Bulge are the same. The carbon-rich and oxygen-rich AGB stars form one population; the differences between the distributions of the two groups are governed mainly by the metallicity gradient. There seems to be a small population that has a distinctly large scaleheight.

All trends in the AOSP sample can be seen in Fig.1 in a pictorial fashion. The exact numbers for the scales in Table 1 should be used with care, since our deprojection method is indirect. Nevertheless, from modelling distribution functions for various of the samples used here the same trends numbers emerge (Sevenster 1997). Also, the scales in the Bulge region agree very well with those recently found from DENIS data (Gilmore priv.comm.).

4 THE BAR

4.1 Surface density

In this section, we compare parametrized bar models to the surface density of the AOSP sample. We do not optimize fits quantitatively, since the choice of a parametrized bar model is already an arbitrary one. Rather, we take bar models that are known to give good approximations to other observations and see how well they agree with ours.

The viewing angle ϕ is the angle between the Bar's major axis and the line of sight toward the galactic Centre (Fig.8(a)). In Fig.8(b,c) we show the surface density distribution as a function of longitude, $N(\ell)$, for two flat (two-dimensional) elliptical bars with gaussian density distribution (cf. G2 model in Dwek et al. 1995). The viewing angles are taken to be 20° , as suggested by some observations (Dwek et al. 1995). The form of $N(\ell)$ depends upon the distance out to which we integrate or, in observational terms, the distance d out to which the data sample the Galaxy, so $N(\ell) = N(\ell; d)$. For values of $d \sim R_\odot$, $N(\ell; d)$ essentially looks like the distribution arising from an $m = 1$ distortion (lopsided; see Fig.8(a)), with its maximum toward *positive* longitudes. With $d = \infty$, however, the distribution is skewed toward *negative* longitudes. This is the result of the line of sight through the $m = 2$ distortion being longer on the far side than on the near side, for small values of absolute longitudes (Fig.8(a)). This effect was first predicted by Blitz & Spergel (1991) and is also seen in the micro-lensing

maps calculated by Evans (1994). The strength of this effect obviously depends upon the parameters of the density distribution of the bar.

We will try to find this effect in our Bulge AOSP sample. The double-peaked OH/IR stars are divided into two equally-sized samples by outflow velocity, at $V_{\text{exp}} = 14$ km s^{-1} , with average V_{exp} of 11.3 (sample I) respectively 18.3 (sample II) km s^{-1} (cf. Fig.1(e,d)). This gives a factor of 1.7 difference in stellar luminosity L_* , even if we assume $\mu_{\text{I}} = 2\mu_{\text{II}}$ (equation (1)). Blommaert et al. (1997) find a range in μ of ~ 2 in the GC with IR observations. The range of masses in the Bulge (Sect.2) makes a factor of 1.7 difference in L_* (~ 1.5 in M_\odot) very well possible. Since the OH masers are saturated, the OH luminosity L_{OH} increases, on average, linearly with L_* . The lower limit to the flux density S_{OH} is the same for both samples, so the average limiting distance of sample II is a factor ~ 1.3 larger than of sample I. We can thus use the two samples to mimic the different integration limits in Fig.8 (see also Sect.2).

The effect of skewed distributions should be clearest in the inner regions of the Galaxy (see Fig.8(b,c)). The ratios of the number of stars with $0^\circ < \ell < 4^\circ$ to the number of stars with $0^\circ > \ell > -4^\circ$ are 39/35 (sample I) and 22/35 (sample II). These ratios are in accordance with the theoretical results shown in Fig.8. To define these trends in a more sophisticated way, we sorted both samples on *absolute* longitude and calculated the cumulative sums of the sign of the longitude $\sum(\ell/|\ell|)$; we add or subtract 1 for each star (Fig.9). An axisymmetric distribution gives a line that hovers around zero. If negative (positive) longitudes are 'overpopulated' the sum will steadily decay (rise). This sum is shown in Fig.9 for the two data sets and for the bar model shown in Fig.8(c), as well as for an N-body model (Fux 1997) found to represent the AOSP sample well (Sevenster et al. 1999). The dotted curves give the 95% confidence limits for deviation from axisymmetry. Sample I (solid curve) never deviates significantly from axisymmetry, although there are local trends similar to those of the models with the intermediate cut-off. Sample II (dashed curve), however, lies at or outside the 5% confidence level and coincides remarkably well with the models without distance cut-off. The set of stars with low V_{exp} would have an average distance cut-off of 9-9.4 kpc according to these models, the set with high V_{exp} of around 12 kpc, beyond which there is no significant contribution from the bar to the integrated density anymore. This agrees very well with the difference of a factor 1.3 in average distance derived from the relation between V_{exp} and stellar luminosity.

We estimate the disk contamination to be $\lesssim 20\%$ within 5° of longitude from the GC (Sect.2; Sevenster 1997). If an axisymmetric component contributes significantly in the inner degrees, the evidence for the existence of the Bar would only become stronger. The $\sum(\ell/|\ell|)$ distribution would not change with the subtraction of a projected axisymmetric distribution of any relative density, but $N(\ell < \ell_{\text{lim}})$ would become lower. This would make the probability of the deviation coming from a binomial distribution even smaller. In other words, the dotted curves in Fig.9 would shift horizontally to the right, but the data-lines would remain in place on average.

The evidence presented here is the first large-scale morphological evidence for a galactic Bar that cannot also be

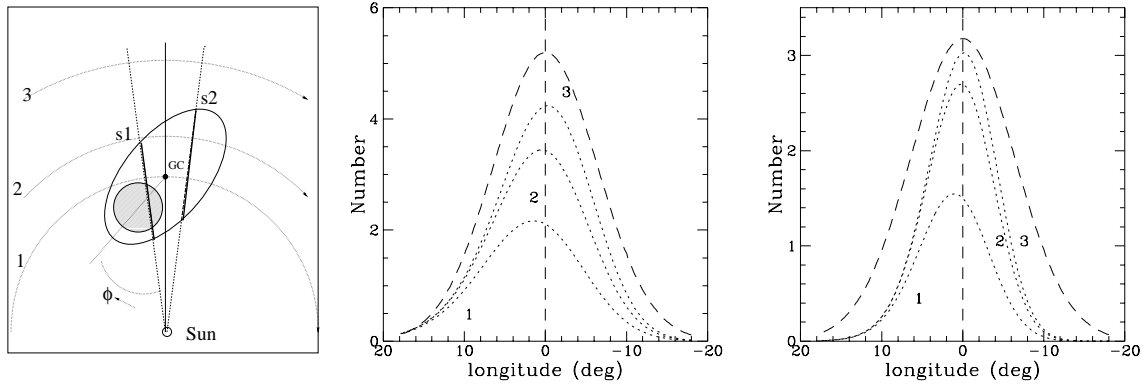


Figure 8 **a** (left) Schematic view of the Bar from the galactic North pole. The viewing angle ϕ is indicated; the near end of the Bar is most certainly at positive longitudes. The lines of sight (s1 and s2) at equal but opposite longitudes differ in length. The dotted arcs show schematically possible observation limits. The shaded circle represents a lopsided distortion, that would project to a similar surface-density distribution as the Bar for an observation limit of R_{\odot} (dotted arc 1). In **b** and **c** we show the total number of stars (arbitrarily normalized) along the line of sight in a two-dimensional elliptical bar model with gaussian density distribution for three different integration limits (8 kpc (1), 9 kpc (2) and ∞ (3); $R_{\odot} \equiv 8$ kpc). The integration limits correspond to the observational limits shown in **a**. For reference a gaussian is shown (dashed). Note the offset of the maximum toward negative longitudes for the largest integration limit. **b** (middle) Axis ratio $q=0.6$, semi-major axis $a=3.5$ kpc ($=3\sigma_{\text{gaus}}$). **c** (right) Axis ratio $q=0.4$, semi-major axis $a=2.5$ kpc ($=3\sigma_{\text{gaus}}$). The viewing angle ϕ is 20° in both panels **b** and **c**. The model in **c** is based on the K-band G2 model for $R_{\text{max}} = 2.4$ kpc of Dwek et al. (1995).

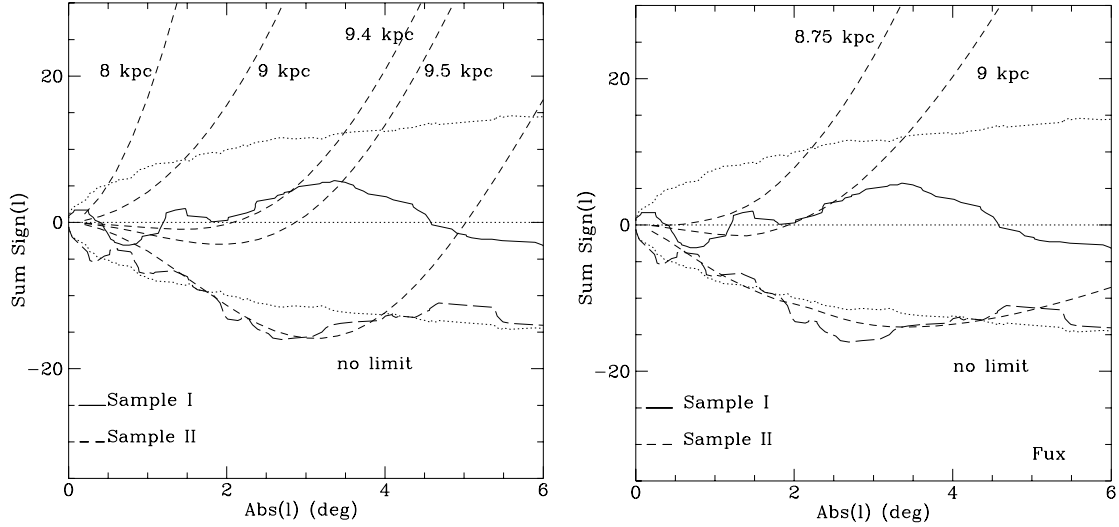


Figure 9 **a** (left) The cumulative sum $\sum(\ell/|\ell|)$ versus $|\ell|$ after sorting on $|\ell|$ for the two samples (thick solid and dashed lines) and for the G2-bar model from Fig.8(c) with different integration cut-offs (short dashed lines, see Fig.8). The dotted curves indicate the values for which the probability of the sum arising in a binomial distribution being larger (or smaller for negative values) than that value is 5% (ie. single-sided). For $|\ell| < 0.5^\circ$ and $|\ell| > 5^\circ$ contributions by additional features influence the distribution (see Fig.1; Sect.5). **b** (right) Same as **a**, but for a bar model consisting of two exponential elliptical-bar profiles with major-axis scalelengths of 200 pc and 1 kpc (central-density contrast 8.5), with viewing angle of 45° and axis ratio of 0.5. The profile is an approximate fit to the density in the plane of an N-body bar and the viewing angle of 45° optimizes the fit between the AOSP data and the N-body model (Sevenster et al. 1999; Fux 1997).

explained by a physical lopsided density distribution (Sevenster 1996). The effect is also clearly visible in Fig.1(b,c) (sample II,I) in a qualitative way. The same trend in the longitude distribution is reported by Unavane & Gilmore (1998) who use L-band data in the plane. However, the necessary extinction corrections are estimates and of similar order as

the asymmetries one is after. Unavane & Gilmore (1998) find that the Dwek models (E2, G3) give too large a deviation from axisymmetry, whereas the G2 model gives a good representation of our data (Fig.9(a)). The results in Fig.9 demonstrate that only for a given density model the parameters of a bar can be optimized (Zhao 1997), as both rather

different models give good representations of the data.

4.2 The Bulge’s kinematic type

The anisotropy parameter (Binney 1976) is a measure of the rotational support of a system. It is the ratio of the maximum rotational velocity of a bulge (V_m) to its central velocity dispersion (σ_0). In combination with the flattening ϵ , it provides a way to distinguish between rotationally-supported, dispersion-supported and streaming-dominated systems (Illingworth 1977). The maximum rotation velocity of the Bulge occurs at $\ell \sim -18^\circ$, where the mean-velocity curve levels out (Fig.10), so $V_m = 140 \pm 20 \text{ km s}^{-1}$. For σ_0 , we use 153 km s^{-1} (Blum 1996), which is more reliable than our determination of this second-order moment ($135 \pm 20 \text{ km s}^{-1}$, Fig.10(b)). This gives a value of V_m/σ_0 of 0.9 ± 0.1 . Together with an ellipticity of $\epsilon \sim 0.4$ (Table 1; Dwek et al. 1995, G0-model; Kent 1992), this locates the galactic Bar in the $V_m/\sigma_0 - \epsilon$ diagram between the oblate and the SAB bulges (Kormendy 1993), governed by somewhat more-than-rotational support. The Galaxy fits well in the relation as an average SAB galaxy.

Earlier values for the Bulge’s dispersion, from measurements toward Baade’s window, were much lower ($113_{-5}^{+6} \text{ km s}^{-1}$; Sharples, Walker & Cropper 1990). Adopting this as σ_0 , the Bulge would be located in the region of extremely triaxial bulges in the $V_m/\sigma_0 - \epsilon$ diagram. Baade’s window ($b = -4^\circ$) is too far from the plane to sample the central Bar dispersion. We conclude that the Bar is so flat that it cannot be assumed to be the dominant contributor to the distribution along the line of sight toward Baade’s window (Table 1; see also Sevenster et al. 1999). Paradoxically, using the dispersion in Baade’s window one would obtain an anisotropy parameter indicative of a strong bar.

5 RESONANT STRUCTURES

In this section, we will concentrate on local features in the distributions of various tracers. For the AOSP sample, these structures are seen in Fig.1, marked as R_{-1} , R_{-2} and R_{-3} . We complement our own evolved-stellar data set with 2.4-GHz-continuum observations (Duncan et al. 1995) and a sample of star-forming regions (Comeron & Torra 1996). The synchrotron radiation dominating the continuum at 2.4 GHz, is found to be a good tracer of the current locations of density waves (eg. Tilanus & Allen 1989).

Duncan et al. (1995) present their data separated in a small-scale- (sub-degree) and large-scale distribution (Fig.11). The small-scale emission arises largely in supernovae; the large-scale emission traces the molecular gas and density waves. For the uninitiated, an introduction to non-axisymmetric galactic dynamics can be found in Binney & Tremaine (Ch.6), and an introduction to terminology and literature in Sevenster (1997).

5.1 The corotation region

The only direct method to find corotation (CR), via the pattern speed, is in most cases inapplicable (see Tremaine & Weinberg 1984; Merrifield & Kuijken 1995). However, a number of indirect indicators can be used. A signature of CR is often observed in the form of dust lanes,

spiral-arm bifurcations or local decreases in the density (eg. Elmegreen 1996). A flat part of the rotation curve may outline roughly the region between the inner-ultra-harmonic resonance (IUHR) and CR (Wozniak & Pfenniger 1997). This is observed in the edge-on S0-galaxy NGC 4570 (van den Bosch & Emsellem 1998). Similarly, the orbital stochasticity in this region (Contopoulos & Grosbøl 1986) will cause efficient radial mixing, smearing out the density gradient (see also Fux 1997). An easily observed result of the dynamics in this region are “inner rings” that are prominent in the majority of barred galaxies (see Buta 1996).

All these features are in fact present in the Galaxy. The narrow gap between the so-called 3-kpc and Norma arms (Fig.11), also seen in other tracers (eg. CO, Bronfman 1992), could well indicate CR. In good agreement with this is that the flat part of the rotation curve found for the AOSP sample (Fig.10) stretches from $\ell \sim -18^\circ$ to $\ell \sim -25^\circ$. Those longitudes would, according to Wozniak & Pfenniger (1997), indicate IUHR and CR, respectively. The very flat density found for this region in Sect.3 further reinforces this picture (Contopoulos & Grosbøl 1986). It also rules out the possibility that the rotation curve is flat due to a logarithmic potential (density $\propto R^{-2}$).

Most importantly, we argue that the 3-kpc arm is the projection not of a spiral arm but of an inner ring, such as mentioned above, for the following reason. A subsample of the AOSP sample follows exactly the longitude-velocity structure of the 3-kpc filament (Fig.12). A group of nine young (high-outflow) stars, that trace the kinematic structure between $0^\circ > \ell > -10^\circ$, stands out in the left panel of Fig.12. These nine stars are at very low latitudes and have a very high median outflow velocity of 17.5 km s^{-1} . If the metallicity is the same as in the rest of the disk, the initial masses of this 3-kpc sample would be $\sim 6 M_\odot$ and the ages $\sim 600 \text{ Myr}$ (Appendix A). As those stars remain close to the gas for several galactic years, their trajectories must follow closely that of the gas. In other words, the gas filament must outline closed orbits instead of a (temporary) spiral density-wave maximum. With proper motions for these stars one could constrain the motion along the 3-kpc arm completely, something that is impossible to achieve with gas.

In Fig.13(a), we show longitude-velocity trajectories constructed by Mulder & Liem (1986). They solved gas-dynamical equations in a weakly-barred potential, using a finite-difference, hydrodynamic grid code. The gas is described by the inviscid Euler equations. The curves in Fig.13(a) represent their preferred model for the 3-kpc arm, the main feature used to constrain the scales of their models. The viewing angle is $\phi = 20^\circ$ and $R_{CR} = 0.98 R_\odot$. In Fig.13(b), the model spiral is seen face-on. Although this spiral reproduces the 3-kpc filament around $\ell=0^\circ$ very well, the tangent point to the 3-kpc arm is at much too high longitude, $\ell = -27^\circ$ (Fig.13(a)). Mulder & Liem (1986) show the longitude-velocity diagram for another model, for $\phi = 40^\circ$ and $R_{CR} = 0.56 R_\odot$. In this diagram the tangent point is much closer to the observed point (see Fig.12) and also the central CO-disk’s velocity signature is matched much better. The trajectories of both ILR arms remain similar in the inner regions. Unfortunately they do not give trajectories for this model but they note that the arms are “more concentrated around CR”. This would be in agreement with our inner ring, discussed above. The Mulder-Liem models are

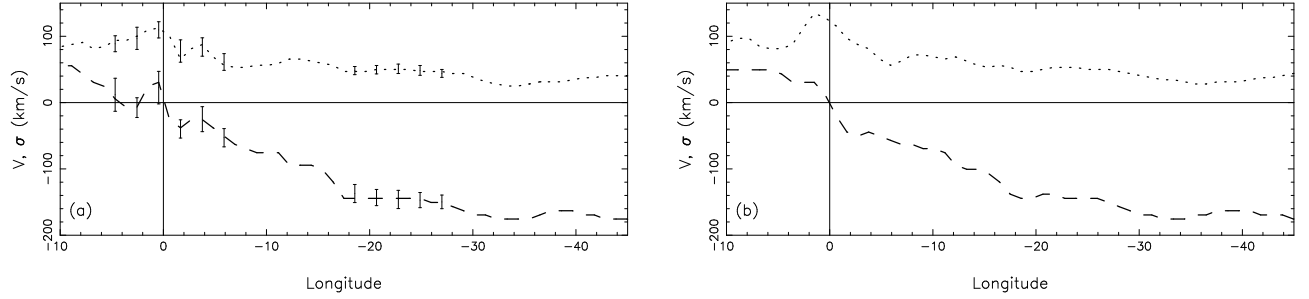


Figure 10 The mean line-of-sight velocity (dash) in the inertial frame (for $V_{\text{LSR}} \equiv 200 \text{ km s}^{-1}$) smoothed data (double-peaked stars only) at $b = 0^\circ$ (a) and $b = 2^\circ$ (b). The gridsize is 1° by 6 km s^{-1} , the initial kernel sizes are 1° and 30 km s^{-1} , respectively. We show errors derived via bootstrapping (Press et al. 1992, see Sevenster 1997) for the features that we discuss in the text. (The mean velocity is the 50% value and dispersion is half the difference of the 83% and the 17% values of the smoothed velocity profiles.)

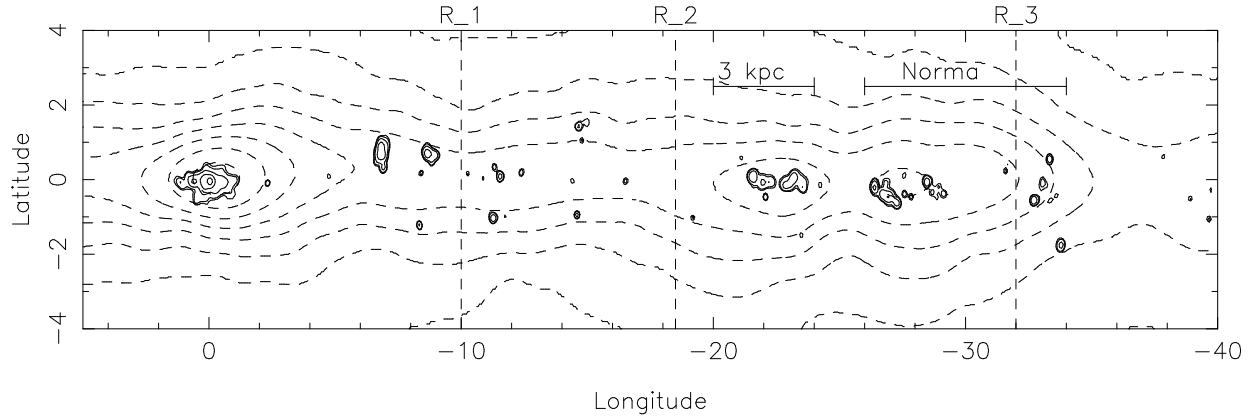


Figure 11 The observed surface-density distribution at 2.4 GHz due to Duncan et al. (1995). The features R_{-1} , R_{-2} and R_{-3} are indicated (see Fig.1) as well as the “Norma arm” (tangent point -32°) and the “3-kpc arm” (tangent point -22°). For the large-scale ($> 1^\circ$) distribution, the ten dashed contours are spaced linearly between 10% and 100% of the maximum (large-scale) density. For the small-scale ($< 1^\circ$) distribution, the ten solid contours are spaced logarithmically between 3% and 95% of the maximum (small-scale) density. The large-scale emission is a good tracer of density waves.

forced to be quasi steady. Therefore, gas flows around CR would not be represented correctly and it could well be that the two arms in Fig.13(b) connect in reality to form a ring.

Binney et al. (1997) find, deprojecting the COBE map with imposed eight-fold symmetry, two density enhancements on the minor axis at 3 kpc from the Centre ($\ell = +17^\circ, -22^\circ$). They suggest these are the $L_{4,5}$ points. With four-fold symmetry, however, they find a, leading, spiral. The longitude $\ell = -22^\circ$ of their feature coincides with the maxima in the OH/IR stars and the 2.4 GHz emission used in this section. As Binney et al. (1997) note, there may be a significant contribution of young stars to the K-band surface density (Rhoads 1996). We argue that their density features are incorrect deprojections of the inner ring. In any case, the derived loci for CR are very similar.

The maxima R_{-2} and R_{-3} interestingly border those of the 2.4 GHz emission (Fig.1). Also, the locations of the maxima in the older and younger OH/IR stars, respectively, are slightly different. Such displacements may be caused by

the intricate streaming and diffusion processes around CR (Roberts, Huntley & van Albada 1979; Kenney & Lord 1991; Vogel et al. 1993; Tilanus & Allen 1989), but it is virtually impossible to draw conclusions from them.

5.2 The inner-Lindblad resonance

Other than a corotation resonance and outer-Lindblad resonances, the existence of an inner-Lindblad resonance (ILR) in a galaxy is dependent on its exact potential. If it exists, it may show via a variety of indicators. The ILR is usually outlined by a “nuclear ring”, often accompanied by massive star formation (see eg. Buta 1996; Phillips 1996). A so-called double-wave feature in the stellar rotation curve (Bettoni 1989) may exist as a result of orbits trapped around the retrograde x_4 orbit family inside ILR (Pfenniger 1984; Wozniak & Pfenniger 1997; Contopoulos & Papayannopoulos 1980). Finally, if an ILR exists, the gas flowing toward the centre, following bar-induced instabilities, will follow offset

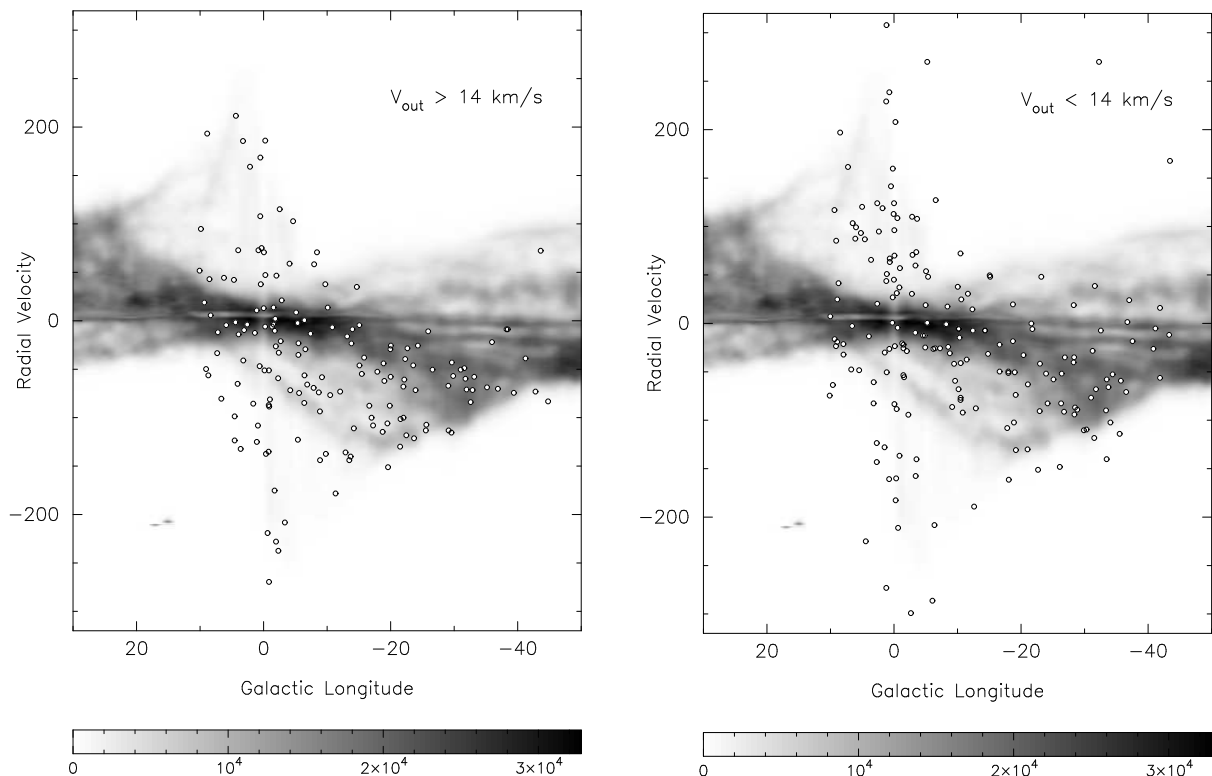


Figure 12 The longitude–velocity diagram for HI (grey scale) in the plane and AOSP stars with $|b| < 1.5^\circ$. Overplotted in the left panel are stars with $V_{\text{exp}} > 14 \text{ km s}^{-1}$ (the young sample) and in the right panel stars with $V_{\text{exp}} < 14 \text{ km s}^{-1}$ (the old sample plus the single-peaked stars). The 3-kpc arm is clearly seen in the HI as the dark linear feature extending from $(+5^\circ, -20 \text{ km s}^{-1})$ to $(-20^\circ, -130 \text{ km s}^{-1})$. The young stars have a subgroup of nine massive stars that follows exactly the longitude–velocity structure of this arm. The old sample shows no connection at all, and deviates in general much more from the HI longitude–velocity diagram. (Courtesy A. Kalnajs)

spiral arms (Athanasoulas 1992). In absence of an ILR, the gas flows to the centre directly along the major axis of the bar.

Comeron & Torra (1996) report an elongated ring-shaped maximum in the deprojected density distribution of ultra-compact HII regions (UCHII). They tentatively identify this with an ILR– or nuclear ring and give radii of 1.3 kpc and 1.9 kpc, for the southern– and northern hemisphere, respectively (corrected for $R_\odot = 8 \text{ kpc}$). In general, these nuclear rings are found to have radii around 1–1.5 kpc (Buta 1996; Freeman 1996).

The radio–continuum distribution (Fig.11) does not show an increase in the number of small-scale sources at $\ell \sim -9.5^\circ$ (1.3 kpc). In that case, star formation must have started too recently for massive stars to become supernovae ($\sim 10^7 \text{ yr}$) and star formation must have ignited between 10^7 yr and $5 \times 10^4 \text{ yr}$ ago (the ages of the UCHII).

A double-wave feature in the OH/IR–star rotation curve can indeed tentatively be identified in Fig.10(a) ($\ell \sim +3^\circ, -4^\circ$). As the AOSP sample is the only large-scale stellar–kinematical sample at low latitudes, it is impossible to verify this feature with other data. According to Woz-

niak & Pfenninger (1997), the deepest minimum in the rotation curve arises around $0.25 R_{\text{CR}}$, when the retrograde orbits remain concentrated around the x_4 family. It is not straightforward to say where the maximum effect will take place in projection; a simple tangent–point assumption is probably not valid. The $\text{Max}(E)$ –model of Wozniak & Pfenninger (1997, see their Figs.4,5) is a good example. In that model, the maximum effect, from the viewing point of the Sun, of this “counter-streaming” comes from the minor axis of the bar. A location on the minor axis at $0.25 R_{\text{CR}}$ would indeed be seen roughly at the longitudes of the observed double-wave feature.

In external barred galaxies, this feature is only seen at intermediate inclinations (Bettoni & Galletta 1997); the Galaxy might be the only edge-on system that allows detection of the double wave, as the disk–foreground contamination is relatively small with respect to other galaxies. Some early-type galaxies are known to harbour kinematically–distinct cores (see eg. Carollo et al. 1997) that can give a similar feature in the rotation curve. The cores contribute a much larger fraction to the total galaxy than do the retrograde orbits mentioned above and so the feature is not so

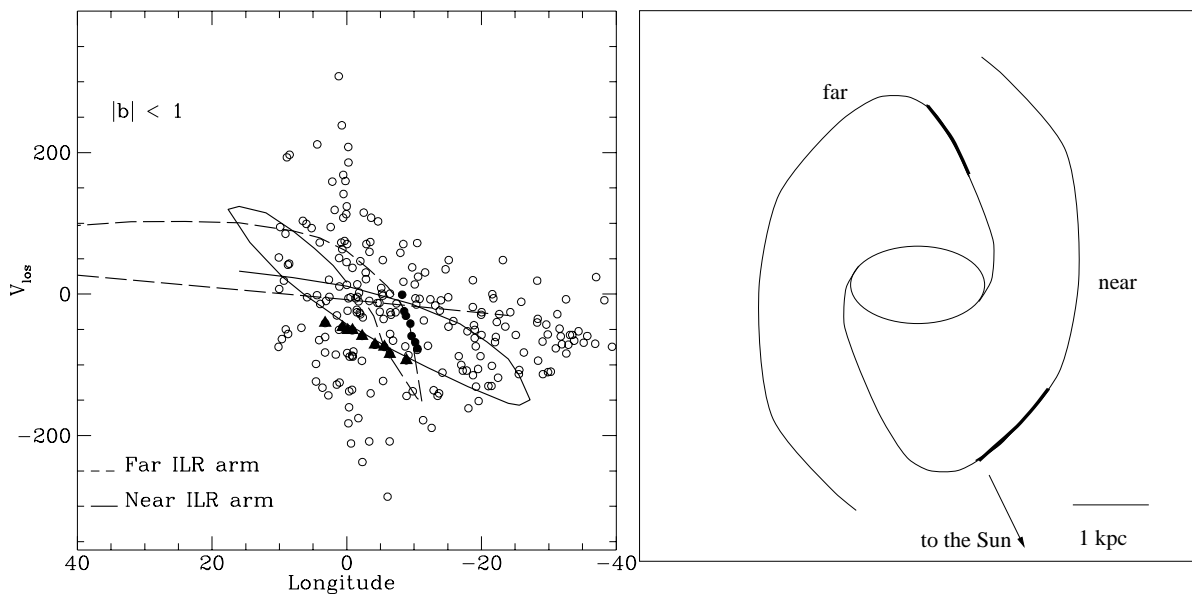


Figure 13 **a** The longitude–velocity diagram for AOSP stars with $|b| < 1^\circ$ (open circles). The filled circles are the 7 stars from R_{-2} with $|b| < 1^\circ$ and the filled triangles the 9 stars connected to the 3-kpc arm. The solid curve is the “near ILR arm” from a model by Mulder & Liem (1986) with $\phi=20^\circ$ and $R_{CR}=0.98 R_\odot$, the dashed curve the “far ILR arm” (see **b**). The velocities are in the inertial frame (changed from Mulder & Liem (1986) for $V_{LSR}=200 \text{ km s}^{-1}$ instead of 250 km s^{-1}). **b** The ILR arms from Mulder & Liem viewed from the galactic North pole. The thickened parts indicate roughly the positions of the two groups of stars marked in **a** if they are connected to those spiral arms. Note that the tangent point to the 3-kpc arm is at too high longitude for the model arm.

easily masked by the foreground disk. We do not think the feature observed in the Galaxy is caused by such a decoupled core because the wave’s velocity maximum and minimum are small with respect to the rotation at large radii. We checked that the feature is not the result of smearing out the effect of the rapidly-rotating galactic-centre OH/IR stars (see Sect.3.2; Lindqvist et al. 1992; Sjouwerma et al. 1998a).

An offset gas flow around ILR would be virtually impossible to detect in the edge-on jungle of the galactic disk. In Fig.13(a), next to the 3-kpc stars, another group of stars is highlighted. The 13 stars forming the feature R_{-1} (Fig.1(e)), seen in the low-outflow, older OH/IR stars only, follow a coherent filament in the longitude–velocity diagram that coincides with part of the far ILR arm (see Fig.13(b)). All 13 stars lie on this filament, although in Fig.13 we have plotted only 7 with $|b| < 0.6^\circ$. (Note that these stars were selected *before* overplotting them on the ILR-arm model.) In Fig.13(b) we indicate roughly where the two small groups of OH/IR stars would be located in the Mulder–Liem model (see Sect.5.1 for caveats concerning this model). The compactness (see Fig.1(e)) of this group of relatively old stars, can indeed be understood more easily if they are spread out along the line of sight as shown. However, the far-advanced age of this group of ILR-arm OH/IR stars is puzzling and prevents us from accepting their location in this picture too readily.

Exemplary of the ILR region in our Galaxy may be the inner region of the galaxy IC 4214 (Hubble type SABab, Saraiva 1996).

6 THE PRESENT SHAPE OF THE INNER GALAXY

The evidence presented in the previous sections may be combined to give the following description of the inner Galaxy (Fig.14). There is a stellar Bar (Sect.4.1) that is fairly flat and weak (Sect.3;4.2). It corotates at $\sim 3.5 \text{ kpc}$ and is surrounded by an inner ring, inside corotation, roughly between 2.5 kpc and 3.5 kpc (Sect.5.1). Possibly an inner-Lindblad resonance exists, with corresponding nuclear ring, between 1 kpc and 2 kpc (Sect.5.2). We suggest that outside corotation a four-armed, trailing spiral exists, which is a bifurcation of a two-armed spiral mode. As such, the Galaxy would be similar in appearance to NGC 1433 (type $(R'_1)SB(rs)ab$; Buta 1995; for a picture see Buta 1996).

If we assume the rotation curve of the axisymmetric part of the Galaxy is described by $184 \text{ km s}^{-1} \text{ kpc}^{-1} R^{0.1}$ (Allen, Hyland & Jones 1983), a pattern speed of $60 \text{ km s}^{-1} \text{ kpc}^{-1}$ is implied for $R_{CR}=3.5 \text{ kpc}$. The radii of ILR, IUHR and OLR in this case are 0.85 kpc , 2.2 kpc and 6.3 kpc , respectively. The radius of ILR depends crucially on the adopted potential and larger radii are easily possible in more centrally concentrated potentials. The radius of IUHR, for $60 \text{ km s}^{-1} \text{ kpc}^{-1}$, agrees well with our suggestion that the inner ring, discussed in Sect.5.1, lies between IUHR and CR. A sudden decrease in metallicity is observed around $R = 6 \text{ kpc}$ (Simpson et al. 1995). If this marks the end of the zone-of-influence of the Bar’s mixing, as suggested by the authors, one expects this to be around OLR. This agrees with the radius of OLR for a pattern speed of $60 \text{ km s}^{-1} \text{ kpc}^{-1}$.

Comparison with published values for the corotation radius and pattern speed proves little conclusive. Values for

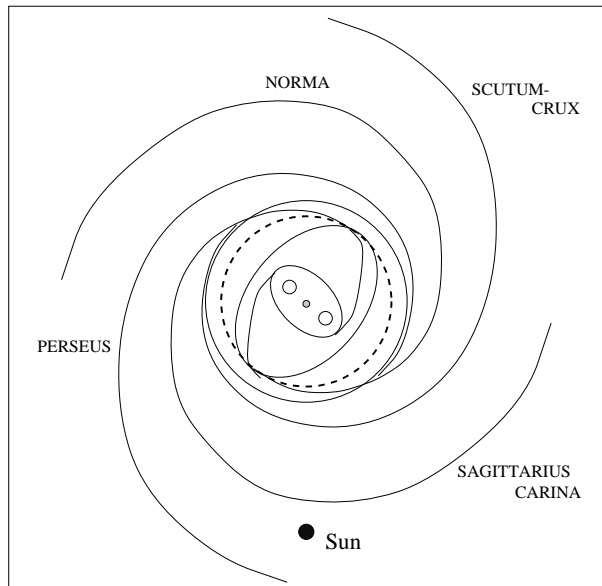


Figure 14 Top-view sketch of the Galaxy as described in Sect.6. The larger ellipse outlines roughly the bar density; the smaller the ILR. The two open circles inside the ILR indicate the loci where the double-wave rotation feature may originate. The short curves emerging from ILR are part of the ILR arms (Mulder & Liem 1986) connecting to IUHR–CR. The thin, solid circle around the bar is CR. The thick dashed ring indicates roughly the IUHR, the inner ring lies between the IUHR– and the CR circle. The spiral arms outside CR are inspired by the picture by Georgelin & Georgelin (1976), structured by the assumption that the four spiral arms are two pairs, bifurcating from one two-armed spiral inside CR. The black dot marks the position of the Sun; the figure is approximately to scale with the distance of the Sun to the galactic Centre (8 kpc). Compare to Fig.6 in de Vaucouleurs & Pence (1978), who sketch a similar view of the Galaxy based on their derived Hubble type (SAB(rs)bc).

corotation range from 2.4 kpc (Binney et al. 1991), 3.5 kpc (Weiner & Sellwood 1996; Englmaier & Gerhard 1999), 4.8 kpc (Fux 1997) to 9 kpc (Amaral & Lepine 1997), and, similarly, for the pattern speed from $19 \text{ km s}^{-1} \text{ kpc}^{-1}$ (Wada et al. 1996) to $118 \text{ km s}^{-1} \text{ kpc}^{-1}$ (Yuan 1984).

6.1 Elongation

In Sect.4.2, we found that the kinematic type of the Bar indicates a rather weakly-barred distribution. This is in agreement with the large in-plane axis ratio of the density, found in several studies: $q_\rho \equiv q_{\Phi''} = 0.6$ (Binney et al. 1997, stellar density) or $q_\rho = 0.7$ (Wada et al. 1996, gas kinematics), although Nikolaev & Weinberg (1997) find $q_\rho = 0.4$. From Fig.9, $q_\rho \sim 0.5$ is not excluded by our data. Due to mixing (Friedli, Benz & Kennicutt 1994), a correlation between the in-plane axis ratio of bars and the metallicity gradient of their host galaxies exists. From an empirical relation between bar axis ratio and $[\text{O}/\text{H}]$ gradient (Martin & Roy 1994), one finds $q_\rho = 0.7$ for a gradient of $-0.07 \text{ dex kpc}^{-1}$ (Smartt & Rolleston 1997).

Inner rings are usually elongated along the bar and follow the shape of the main closed orbits; their axis ratio is $q_{\Phi'}$ (see Buta 1996) and thus – in general – larger than q_ρ . The elongation can be constrained by the radial motion

along the ring. At $\ell = 0^\circ$, the line-of-sight velocity is -53 km s^{-1} , or in other words a radial velocity V_R of $+53 \text{ km s}^{-1}$ (Fig.12; Oort 1977). If this is the line-of-sight component of a streaming along the ring, V_\parallel , we can define an angle $\beta = \arccos(V_R/V_\parallel)$. If we assume further that the ring is an ellipse, with a viewing angle ϕ of the major axis (near end at positive longitudes), and that the streaming is along the ellipse, we can derive the axis ratio q_e via $q_e^2 = \tan(\beta - \phi) \tan \phi$, with $0 \leq \phi < \beta \leq \frac{\pi}{2}$. For $V_\parallel = 200 \text{ km s}^{-1}$, $\beta = 75^\circ$ and we find $q_e = 0.76$ for $\phi = 45^\circ$ ($q_e = 0.75$ for $\phi = 25^\circ$; $q_e = 0.61$ for $\phi = 65^\circ$). For $V_\parallel = 150 - 300 \text{ km s}^{-1}$, $\beta = 70^\circ - 80^\circ$ and $q_e = 0.68 - 0.84$. Hence, for $20^\circ < \phi < 55^\circ$, the observed V_R is consistent with $q_e \equiv q_{\Phi'} > 0.6$ for a wide range of V_\parallel . The largest $q_{\Phi'}$ arises for $\phi = 0.5 \beta$.

In general $q_\Phi > q_{\Phi'} > q_\rho$, so the radial velocity of the 3-kpc arm can be accommodated in an almost-round potential (see also Sil'chenko et al. 1997), contrary to some claims (eg. Mulder & Liem 1986).

7 EVOLUTION OF THE INNER GALAXY

The morphological properties of bars are found to be related to their formation mechanism (Noguchi 1996), to the rotation curve (Combes & Elmegreen 1993) and to the Hubble type of the host galaxy (Elmegreen & Elmegreen 1985). Early-type-galaxy bars ($\lesssim \text{Sb}$ in this context) have flat density profiles and an ILR, end close to their corotation radius and form via strong tidal interaction with other galaxies. Late types ($\gtrsim \text{Sc}$) have exponential density profiles, no ILR, end well inside (sometimes halfway) their corotation radius and form via disk instabilities.

In this section, we will speculate on the formation and evolution of the galactic Bar, and on how it influenced the structure of the inner Galaxy.

7.1 How did the Bar form ?

The Galaxy is usually classified as an Sb or Sbc galaxy in the Hubble sequence (de Vaucouleurs & Pence 1978) and is as such just intermediate to the two classes described above. The Bar's steep density profile (Sect.3.4; Binney et al. 1997) and length ($R_{\text{CR}}/a > R_{\text{CR}}/R_{\text{IUHR}} = 1.4$) indicate a late type. Is it possible that the Bar in our Galaxy indeed formed via disk instability? Studies of Toomre's instability parameter Q (Toomre 1964) show that the Galaxy is (marginally) stable at all radii (Fuchs & von Linden 1997; Lewis & Freeman 1989). Earn & Lynden-Bell (1996) also find that, for the Bulge's present rotation curve $V_c \propto R^{0.1}$ ($\rho \propto R^{-1.8}$, Allen et al. 1983), $m = 2$ modes will not be sustained via orbit cooperation (alignment).

However, in the first gigayears of the life of the Galaxy ($\gg 5 \text{ Gyr}$ ago), when the stellar dispersions had not yet increased to their maximum value (Freeman 1991), the disk was probably unstable (Fuchs & von Linden 1997). Especially if there was a weak trigger (the Large Magellanic Cloud, Weinberg 1996) it is possible that the Bar formed via a disk instability, more than 5 Gyr ago. The strong correlation between kinematics and metallicity (eg. Zhao, Spergel & Rich 1994) favours secular bar formation and thus excludes strong interaction as a mechanism, pointing to a disk-bar connection rather than to a halo-bar connection. The similar scaleheights for the two components found in Sect.3 (Table

1) support a disk–bar connection and the formation of the bar from the disk via a planar instability.

7.2 When did the Bar form ?

In general, it is suggested that the Bar is a young component with respect to the spheroidal components (Bulge, Halo). Several authors find ages for the Bar of 6 Gyr to 9 Gyr (Ng et al. 1996; Gerhard & Binney 1993; Wyse, Gilmore & Franx 1997). The OH/IR stars in the direction of the Bar have an upper age limit of 7.5 Gyr (Sect.2). If these OH/IR stars are the result of renewed star formation in response to the formation of the Bar (see discussion Sect.7.3), then the Bar must be at least 8 Gyr old. Such an age might allow for the disk–instability formation mechanism (see above). The scenario of Ng et al. (1996; their Fig.13) explains the absence of very old Bulge OH/IR stars and the similarity of the metallicity of OH/IR stars in the Bar and in the Disk (Sect.2). The absence of Bulge OH/IR stars older than 7.5 Gyr indicates that the already existing old Bulge (>13 Gyr; Ng et al. 1996; Wyse et al. 1997) was not forming significant numbers of 1–6 M_{\odot} stars in the plane in this era.

7.3 What happened next ?

Of special interest is the bar–induced mass flow to the central regions of galaxies (Hasan, Pfenniger & Norman 1993; Wada & Habe 1992,1995) that has strong influence on the evolution of the bar itself, eventually resulting in its destruction. Wada & Habe (1992, 1995) find that the presence of an ILR is essential, but however, Athanassoula (1992) and Piner, Stone & Teuben (1995) find that more generic mass transport always occurs, even preferentially in systems without ILR.

The gas, flowing to the centre, causes instabilities and star formation. In order to induce Jeans’ instabilities at the scales of giant molecular clouds ($M_J < M_{\text{GMC}}$, eg. Gerritsen & Icke 1997) $10^8 M_{\odot}$ of gas has to be transported to within 100 pc (for $M_{\text{GMC}} = 1 \times 10^6 M_{\odot}$; the masses of the SgrA,B GMCs are $2, 6 \times 10^6 M_{\odot}$, Stark et al. 1991). The observed gas–inflow rate into the central 100 pc is $0.01 M_{\odot} \text{ yr}^{-1}$ (von Linden, Duschl & Biermann 1993) and presumably was higher just after formation of the Bar (eg. Piner et al. 1995). This means it would take less than 10 Gyr, or more or less the estimated age of the Bar, for the central density to build up enough for the onset of central star formation.

Evidence for massive, on–going star formation in the galactic Centre from eg. the presence of H_2O masers has been negated (Sjouwerman & van Langevelde 1996). Nevertheless, the rate inside 500 pc is higher than elsewhere, $\sim 0.5 M_{\odot} \text{ yr}^{-1}$ (Güsten 1989) and the OH/IR stars in the galactic Centre (inside 100 pc) appear to be younger on average than the global population (Sjouwerman et al. 1998b; Blommaert et al. 1997; Wood, Habing & McGregor 1998).

The galactic–centre OH/IR stars have a bimodal distribution of outflows (Fig.4) that differs from that of the Bulge sample with more than 99.9% significance (Kolmogorov–Smirnov). The lower outflow velocities are distributed in a rather wide range (26% fractional scatter) around 11.4 km s^{-1} , the higher in a narrow range (10%) around 19.4 km s^{-1} . Especially when allowing for a scatter in the metallicity, the masses of the high–outflow galactic–centre stars

must span a relatively narrow range as well (Appendix A). This suggests a short episode of star formation, which according to Sjouwerman et al. (1998b) took place more than 1 Gyr ago. The two groups of galactic–centre OH/IR stars are separated roughly by $V_{\text{exp}} = 15 \text{ km s}^{-1}$, corresponding to an age of approximately 1.5 Gyr (Sect.2, Appendix A) for solar metallicity. The sudden horizontal step in the cumulative distribution around 15 km s^{-1} suggests that around 1.5 Gyr ago there was either a sudden increase of the ambient metallicity or of the average mass of the formed stars. Observations show that the high–outflow galactic–centre OH/IR stars have metallicities of a factor of two higher than the low–outflow– and the Bulge objects (Blommaert et al. 1997; Wood et al. 1998). Hence, in the case of a burst starting 1.5 Gyr before present, the progenitor masses of the present high–outflow population must have been well over $3 M_{\odot}$ (Bertelli et al. 1994), in good agreement with Wood et al. (1998). For twice–solar metallicity, the luminosity of these objects would be $\sim 90\%$ of the average luminosity of the Disk AOSP stars (Bertelli et al. 1994) which, with the high outflow velocities, agrees well with equation (1). Sjouwerman et al. (1998b) find that in total more than $10^7 M_{\odot}$ of stars would have formed in the starburst. However, they use half–solar metallicities in which case the luminosity would be $\sim 110\%$ of the Disk AOSP stars (still for ages of 1.5 Gyr). Such a model does not satisfy equation (1) at all. As this model uses lower progenitor masses, we conclude that in our high–metallicity scenario the burst would be a factor of five times more massive than estimated by Sjouwerman et al. (1998b).

More recent (~ 7 Myr and ~ 100 Myr ago) and much less massive starbursts are reported by Krabbe et al. (1995). These are too recent to show up in the outflow–velocity distribution of the OH/IR stars.

7.4 The complete scenario

The following speculative scenario emerges. The Bar formed ~ 8 Gyr ago via a disk instability. Subsequent gas flows revived star formation in the Bulge region and the progenitors of the present–day Bulge OH/IR stars started to form. The metallicity in the inner plane became similar for all radii. Enriched material kept flowing into the central 100 pc, from the region inside corotation, and around 1.5 Gyr ago, a star burst ignited, leaving a significantly more metal–rich population in the galactic Centre.

Another possible consequence of the build–up of mass in the centre is the formation of an ILR, typically when the mass inside 200 pc is 1–2% of the mass of the galaxy (Friedli & Benz 1993). The ring of UCHIIs (Sect.5.2) could indicate that an ILR exists in the Galaxy, and that has formed recently because it is not seen in any older (>10 Myr) population. The critical density for a nuclear–ring star burst is $0.6\kappa^2/G$ (Elmegreen 1994a,b), yielding a required ring mass of $\lesssim 1 \times 10^8 M_{\odot}$ which could have accumulated from the inflowing gas in ~ 1 Gyr, once the ILR formed ($0.1 M_{\odot} \text{ yr}^{-1}$, Friedli & Benz 1993, for $q_p = 0.7$). The ILR would hence have formed coevally with the central star burst derived from the OH/IR star population.

The total mass within 100 pc is $> 5 \times 10^8 M_{\odot}$ (Lindqvist et al. 1992; Kent 1992). This is $\sim 3\%$ of the total mass of the Bulge ($\sim 2 \times 10^{10} M_{\odot}$; Zhao 1996; Blum 1995; Kent

1992). Such a concentration is sufficient to destroy the Bar completely (Hasan et al. 1993).

The ILR may slow down the self-destruction of the Bar, by decreasing the rate of gas flow to the centre, but does not stop it (Hasan et al. 1993; Piner et al. 1995). In addition, inside ILR no bar-supporting orbits would exist (Contopoulos & Papayannopoulos 1980). With already an almost-critical amount of mass in the central regions, the Bar may be completely dissolved within a few Gyr.

A view of the possible future of the Galaxy can be obtained by looking at NGC 7217 (Athanasoula 1996). This galaxy has an inner, an outer and a nuclear ring, but no clear bar. It may be a remnant of a once-barred galaxy that dissolved, which could also account for the high fraction (25%) of counter-rotating orbits in this galaxy (Merrifield & Kuijken, 1994).

The observed CO parallelogram (Bally et al. 1988) was elegantly explained as the inner cusped x_1 orbit by Binney et al. (1991). However, Liszt & Burton (1978) already showed that the parallelogram is most likely the result of a tilt in the inner CO distribution. In this case, the constraint, placed on the Bar's parameters by identifying this inner cusped x_1 orbit (yielding a very low viewing angle and corotation radius), can be lifted. In our scenario, the CO would be on x_2 orbits inside ILR.

8 CONCLUSIONS

We have given several new arguments in favour of the triaxiality of the central Galaxy. In the inner 10° , perspective effects provide evidence for the existence of a Bar. More indirect evidence comes from the presence of resonant features. We argue that an inner ring, with a flat density distribution and rotation curve, and a gap in the Norma-arm region indicate the region inside corotation. A possible nuclear ring and a double-wave feature in the stellar rotation curve are indicative of the existence of an inner-Lindblad resonance. We find that corotation is at 3.5 kpc, the bar ends within 2.5 kpc (IUHR) and the pattern speed is $\sim 60 \text{ km s}^{-1} \text{ kpc}^{-1}$. The radius of the ILR is most likely larger than what would be derived from a $R^{0.1}$ rotation curve (Allen et al. 1983).

The much-studied 3-kpc arm is probably an inner ring, connected to the IUHR-CR region rather than OLR (Yuan 1984; Binney et al. 1991) or ILR (Amaral & Lepine 1997). Its radial motion at $\ell = 0^\circ$ can be explained well by streaming along mildly elongated closed orbits ($q > 0.7$) for a wide range of viewing angles.

The galactic Bar is no extraordinary specimen. The value of the anisotropy parameter V_m/σ_0 and flattening ϵ define it as an SAB-bulge. The Hubble type of the Galaxy is SAB(rs)b (and possibly an additional (nr) for the nuclear ring), based on its axis ratio, its spiral and ring structure and its kinematic type (cf. SAB(rs)bc, de Vaucouleurs & Pence 1978).

Based on the maximum ages of the OH/IR stars in the direction of the Bulge, we speculate that the Bar's formation took place ~ 8 Gyr ago. Induced mass flow to the centre changed the mass distribution significantly. As a consequence, at ~ 1.5 Gyr ago a major star burst ignited (within 100 pc) and an ILR formed. The Bar could be in the final stage of its existence.

The OH/IR stars in our sample at low latitudes are all part of the intermediate-age Bar and do not trace the old, axisymmetric Bulge mentioned by eg. Ng et al. (1996) and Wyse et al. (1997). The Bar determines, via its influence on the metallicity gradient, the radial distribution of AGB stars in the disk (~ 0.5 to $1.5 R_\odot$), as the ratio of oxygen-rich to carbon-rich AGB stars is governed by the metallicity gradient. These two groups together form one population in terms of their galactic distribution. The AGB stars are distributed in the thin (old) disk with a scaleheight of 100 pc for the youngest AGB stars ($\lesssim 1$ Gyr) and 500 pc for AGB stars older than $\gtrsim 5$ Gyr. There is possibly a disjunct 1-kpc-scaleheight population of OH/IR stars, that is seen only very locally ($\ell \sim 50^\circ$) and is between 1 Gyr and 10 Gyr old (depending on metallicity).

ACKNOWLEDGMENTS

I am grateful to the following people for their continued interest, their very helpful discussions, ideas, suggestions and for spotting easily-overlooked mistakes: Richard Arnold, Frank van den Bosch, Butler Burton, Carsten Dominik, Ron Ekers, Harm Habing, Vincent Icke, Agris Kalnajs and Tim de Zeeuw. Roger Fux made an N-body model available (Fig.9) and Lorant Sjouwerman OH/IR star data (Fig.4), both before publication. I also thank Janet Soulsby and Neil Killeen for helping improve my usage of the English language.

REFERENCES

- Amaral L., Lepine J., 1997, MNRAS 286, 885
- Allen D., Hyland A., Jones T., 1983, MNRAS 204, 1145
- Athanasoula E., 1992, MNRAS 259, 345
- Athanasoula E., 1996, In: Buta, Crocker, Elmegreen (eds.) PASPC 91, Barred Galaxies, p. 309
- Bally J., Stark A., Wilson R., Henkel C. 1988, ApJ 324, 223
- Baud B., Habing H., Matthews H., Winnberg A., 1981, A&A 95, 156
- Bettoni D., 1989, AJ 97, 79
- Bettoni D., Galletta G., 1997, A&AS 124, 61
- Bertelli G., Bressan A., Chiosi C., Fagotto F., Nasi E., 1994, A&AS 106, 275
- Binney J.J., 1976, MNRAS 177, 19
- Binney J.J., Tremaine S., 1987, Galactic Dynamics, Princeton University Press (BT)
- Binney J.J., Gerhard O., Stark A., Bally J., Uchida K., 1991, MNRAS 252, 210
- Binney J.J., Gerhard O.E., Spergel D.N., 1997, MNRAS 288, 365
- Blanco V., 1965, In: Blaauw A., Schmidt M. (eds.) Galactic Structure. Chicago, p. 241
- Blitz L., Spergel, D., 1991, ApJ 379, 631
- Blommaert J., Veen W. van der, Habing H.J., 1993, A&A 267, 39
- Blommaert J., Veen W. van der, Langevelde H. van, Habing H.J., Sjouwerman L.O., 1997, A&A 329, 991
- Blum R., 1995, ApJ 444, L89
- Blum R., 1996, PASP 108, 223 (dissertation summary)
- Bronfman L., 1992, In: Blitz (ed.) The Center, Bulge and Disk of the Milky Way. Kluwer, Dordrecht, p. 131
- Buta R., 1995, ApJS 96, 39
- Buta R., 1996, In: Buta, Crocker, Elmegreen (eds.) PASPC 91, Barred Galaxies, p. 11
- Carollo C.M., Franx M., Illingworth G., Forbes D., 1997, ApJ 481, 710

- Chengalur J., Lewis B., Eder J., Terzian Y., 1993, *ApJS* 89, 189
- Combes F., Elmegreen B., 1993, *A&A* 271, 391
- Cameron F., Torra J., 1996, *A&A* 314, 776
- Contopoulos G., Papayannopoulos T., 1980, *A&A* 92, 33
- Contopoulos G., Grosbøl P., 1986, *A&A* 155, 11
- de Grijs R., Peletier R., 1997, *A&A* 320, L21
- de Vaucouleurs G., Pence W., 1978, *AJ* 83, 1163
- Duncan A., Stewart R., Haynes R., Jones K., 1995, *MNRAS* 277, 36
- Dwek E. et al. 1995, *ApJ* 445, 716
- Earn D., Lynden-Bell D., 1996, *MNRAS* 278, 395
- Elmegreen B., Elmegreen D., 1985, *ApJ* 288, 438
- Elmegreen B., 1994a, *ApJ* 425, L73
- Elmegreen B., 1994b, In : Tenorio-Tagle (ed.), *Violent Star formation – From 30 Dor to QSOs*. Cambridge
- Elmegreen B., 1996, In: Buta, Crocker, Elmegreen (eds.) *PASPC 91, Barred Galaxies*, p. 197
- Englmaier P., Gerhard O., 1999, *MNRAS* 00, 000 (astro-ph 9810208)
- Evans N.W., 1994, *ApJ* 437, L31
- Freeman K., 1991, In : Sundelius (ed.) *Dynamics of disk galaxies*. Sweden, p.15
- Freeman K., 1996, In: Buta, Crocker, Elmegreen (eds.) *PASPC 91, Barred Galaxies*, p. 1
- Friedli D., Benz W., 1993, *A&A* 268, 65
- Friedli D., Benz W., Kennicutt R., 1994, *ApJ* 430, L105
- Frogel J., 1988, *ARA&A* 26, 51
- Fuchs B., von Linden S., 1998, *MNRAS* 294, 513
- Fux R., 1997, *A&A* 327, 983
- Garcia Lario D.P., 1991, dissertation Instituto de Astrofísica de Canarias
- Georgelin Y., Georgelin Y., 1976, *A&A* 49, 57
- Gerhard O., Binney J., 1993, In: Dejonghe H., Habing H.J. (eds.) *Proc. IAU Symp. 153, Galactic Bulges*. Reidel, Dordrecht, p. 275
- Gerhard O., 1996, In: Blitz L., Teuben P.(eds.) *Proc. IAU Symp. 169, Unsolved problems of the Milky Way*. Reidel, Dordrecht, p. 79
- Gerritsen J., Icke V., 1997, *A&A* 325, 972
- Gilmore G., Reid N., 1983, *MNRAS* 202, 1025
- Güsten R., 1989, In: Morris M.(ed.) *Proc. IAU Symp. 136, The Centre of the Galaxy*. Kluwer, p. 89
- Habing H.J., 1988, *A&A* 200, 40
- Habing H.J., 1993, In: Dejonghe H., Habing H.J. (eds.) *Proc. IAU Symp. 153, Galactic Bulges*. Reidel, Dordrecht, p. 57
- Habing H.J., Tignon J., Tielens A., 1994, *A&A* 286, 523
- Hasan H., Pfenniger D., Norman C., 1993, *ApJ* 409, 91
- Ibata R., Gilmore G., 1995, *MNRAS* 275, 605
- Illingworth G., 1977, *ApJ* 218, L43
- Kenney J., Lord S., 1991, *ApJ* 381, 118
- Kent S., Dame T., Fazio G., 1991, *ApJ* 378, 131
- Kent S., 1992, *ApJ* 387, 181
- Kormendy J., 1993, In: Dejonghe H., Habing H.J. (eds.) *Proc. IAU Symp. 153, Galactic Bulges*. Reidel, Dordrecht, p. 209
- Krabbe A. et al. 1995, *ApJ* 447, L95
- Lewis J., Freeman K., 1989, *AJ* 97, 139
- Lindqvist M., Habing H.J., Winnberg A., 1992, *A&A* 259, 118
- Liszt H., Burton W., 1978, *ApJ* 226, 790
- Loup C., Forveille T., Omont A., Paul J., 1993, *A&AS* 99, 291
- Martin P., Roy J., 1994, *ApJ* 424, 599
- Merrifield M., Kuijken K., 1994, *ApJ* 432, 575
- Merrifield M., Kuijken K., 1995, *MNRAS* 274, 933
- Merritt D., Tremblay B., 1994, *ApJ* 108, 514
- Mihalas , Binney J., 1981, *Galactic Astronomy*
- Mulder W., Liem B., 1986, *A&A* 157, 148
- Ng Y., Bertelli G., Chiosi C., Bressan A., 1996, *A&A* 310, 771
- Nikolaev S., Weinberg M., 1997, *ApJ* 487, 885
- Noguchi M., 1996, In: Buta, Crocker, Elmegreen (eds.) *PASPC 91, Barred Galaxies*, p. 339
- Ojha D., Bienayme O., Robin A., Creze M., Mohan V., 1996, *A&A* 311, 456
- Oort J.H., 1977, *ARA&A* 15, 295
- Pfenniger D., 1984, *A&A* 134, 373
- Phillips A., 1996, In: Buta, Crocker, Elmegreen (eds.) *PASPC 91, Barred Galaxies*, p. 44
- Piner B., Stone J., Teuben P., 1995, *ApJ* 449, 508
- Press W., Teukolsky S., Vetterling W., Flannery B., 1992, “Numerical Recipes”, Cambridge University Press
- Rhoads J., 1996, In: Minniti, Rix (eds.) *Spiral galaxies in the NIR*. Heidelberg, p. 58
- Roberts W., Huntley J., Albada G. van, 1979, *ApJ* 233, 67
- Sackett P., 1997, *ApJ* 483, 103
- Saraiva M., 1996, In: Buta, Crocker, Elmegreen (eds.) *PASPC 91, Barred Galaxies*, p. 120
- Sellwood J., Wilkinson A., 1993, *Rep. Prog. Phys.*, 56, 173
- Sevenster M., Dejonghe H., Habing H., 1995, *A&A* 299, 689
- Sevenster M., 1996, In: Buta, Crocker, Elmegreen (eds.) *PASPC 91, Barred Galaxies*, p. 536
- Sevenster M., Chapman J., Habing H., Killeen N., Lindqvist M., 1997a, *A&AS* 122, 79
- Sevenster M., Chapman J., Habing H., Killeen N., Lindqvist M., 1997b, *A&AS* 124, 509
- Sevenster M., 1997, PhD dissertation Leiden University, The Netherlands (copies available upon request to the author)
- Sevenster M., Saha P., Fux R., Valls-Gabaud D., 1999, *MNRAS* 00, 000
- Sharples R., Walker A., Cropper M., 1990, *MNRAS* 246, 54
- Sil’chenko O., Zasov A., Burenkov A., Boulesteix J., 1997, *A&AS* 121, 1
- Simpson J., Colgan S., Rubin R., Erickson E., Haas M., 1995, *ApJ* 444, 721
- Sjouwerman L., Langevelde H. van, 1996, *ApJ* 461, L41
- Sjouwerman L., Langevelde H. van, Winnberg A., Habing H., 1998a, *A&AS* 128, 35
- Sjouwerman L., Habing H., Lindqvist M., Langevelde H. van, Winnberg A., 1998b, in Falcke et al.(eds), *Galactic Center Workshop 1998*, ASP
- Smartt S., Rolleston W., 1997, *ApJ* 481, L47
- Spaenhauer A., Jones B., Whitford A., 1992, *AJ* 103, 297
- Sridhar S., Touma J., 1996a, *MNRAS* 279, 1263
- Sridhar S., Touma J., 1996b, *Sci* 271, 973
- Stark A., Gerhard O., Binney J., Bally J., 1991, *MNRAS* 248, 14P
- Tanabe T., et al. 1997, *Nat* 385, 509
- te Lintel Hekkert P., Habing H., Caswell J., Norris R., Haynes R., 1991, *A&AS* 90, 327
- Tilanus R., Allen R., 1989, *ApJ* 339, L57
- Toomre A., 1964, *ApJ* 139, 1217
- Tremaine S., Weinberg M., 1984, *ApJ* 282, L5
- Unavane M., Wyse R., Gilmore G., 1996, *MNRAS* 278, 727
- Unavane M., Gilmore G., 1998, *MNRAS* 29, 145
- van den Bosch F.C., Emsellem E., 1998, *MNRAS* 298, 267
- van der Veen W., Habing H.J., 1988, *A&A* 194, 125
- van der Veen W., 1989, *A&A* 210, 127
- van der Veen W., Habing H.J., 1990, *A&A* 231, 404
- Vogel S., Rand R., Gruendl R., Teuben P., 1993 *PASP* 105 666
- von Linden S., Duschl W., Biermann P., 1993, *A&A* 269, 169
- Wada K., Habe A., 1992, *MNRAS* 258, 82
- Wada K., Habe A., 1995, *MNRAS* 277, 433
- Wada K., Taniguchi Y., Habe A., Hasegawa T., 1996, In: Buta, Crocker, Elmegreen (eds.) *PASPC 91, Barred Galaxies*, p. 554
- Weinberg M., 1996, In: Buta, Crocker, Elmegreen (eds.) *PASPC 91, Barred Galaxies*, p. 517

- Weiner B., Sellwood J., 1996, In: Blitz L., Teuben P.(eds.) Proc. IAU Symp. 169, Unsolved problems of the Milky Way. Reidel, Dordrecht, p. 145
- Wielen R. 1977, A&A 60, 263
- Wood P., Habing H., McGregor P., 1998, A&A 336, 925
- Wozniak H., Pfenniger D., 1997, A&A 317, 14
- Wyse R., Gilmore G., Franx M., 1997, ARA&A 35, 637
- Yuan C., 1984, ApJ 281, 600
- Zhao H.S., Spergel D.N., Rich R.M. 1994, ApJ 108, 2154
- Zhao H.S., 1996, MNRAS 283, 149
- Zhao H.S., 1997, astro-ph 9705046

Appendix A The luminosity–metallicity–outflow–velocity relation

In this appendix, we outline the derivation of the relation between (unknown) stellar luminosity, outflow velocity and envelope metallicity for OH/IR stars.

We assume a star of luminosity L_* and an isotropic and constant mass outflow \dot{M} . At a distance R_0 the gas temperature has decreased to a value of T_c , equal to the condensation temperature of some solid species. The particles that form are immediately accelerated to their final outflow velocity V_{exp} . Because of friction they take the gas along. We have now the following equation :

$$\dot{M} V_{\text{exp}} = \tau L_*/c \quad (\text{A1})$$

as the momentum change of the outflowing mass equals the radiation pressure on the dust. τ is the dust opacity of the circum–stellar envelope and c the speed of light. Also :

$$\dot{M} = 4\pi R_0^2 \rho_0 V_{\text{exp}} \quad (\text{A2})$$

with ρ_0 the density at radius R_0 . From equation (A2) and the fact that V_{exp} is constant it follows that $\rho = \rho_0(R_0/R)^2$. We then obtain :

$$\tau = \frac{1}{\mu} \kappa_0 \int_{R_0}^{\infty} \rho(R) dR = \frac{1}{\mu} \kappa_0 \rho_0 R_0 \quad (\text{A3})$$

with κ_0 the mean absorption coefficient and μ the gas–to–dust ratio of the circum–stellar envelope. The dust forms when the radiation temperature has fallen to T_c :

$$\sigma T_c^4 = L_*/(4\pi R_0^2) \quad (\text{A4})$$

with σ the Stefan–Boltzmann constant. We have four equations and seven variables (\dot{M} , L_* , μ , τ , R_0 , ρ_0 , V_{exp}) and thus three parameters can be chosen freely. We will take \dot{M} , L_* and μ . It is then easy to show that :

$$V_{\text{exp}}^4 = AL_* \mu^{-2} \quad (\text{A5})$$

where the constant A is given by

$$A = \frac{\kappa_0^2 \sigma}{(4\pi)^3 T_c^4 c^2} \quad (\text{A6})$$

Thus V_{exp} is independent of \dot{M} .

In a more elaborate model one may drop the assumption that the dust acquires its final velocity immediately. The gas is being dragged along by the dust; there will be a drift between those components. Analytic solutions no longer exist

and equation (A5) is slightly different (Habing et al. 1994) :

$$V_{\text{exp}}^{3.3} = AL_* \mu^{-1.7} \quad (\text{A7})$$

By dividing a sample of OH/IR stars into two according to outflow velocity one thus effectively divides the sample into more and less luminous stars. All existing models of AGB–star evolution (eg. Vassiliades & Wood) predict that the more massive a main–sequence star is, the higher its AGB luminosity. Thus stars of high V_{exp} are younger than those of low V_{exp} . This is confirmed by the fact that stars with low V_{exp} have larger scaleheight than those with high V_{exp} (first discussed by Baud et al. 1981).

In principle there could be a conspiracy. The stars with higher V_{exp} could have higher metallicities and lower values of μ . A variation in μ could thus cancel the effect of a variation in V_{exp} and stars with higher V_{exp} would be *older*. However, for OH/IR stars, $\mu \propto Z^{-1}$ (Habing et al. 1994). For the conspiracy to work, $Z \propto V_{\text{exp}}^2$ and Z must differ by at least a factor of four between stars to explain the observed outflow velocities (<10 to >20 km s $^{-1}$). It is therefore unlikely that the conspiracy should influence our conclusion, because the OH/IR stars are younger than ~ 7 Gyr and oxygen–rich and thus have all formed in similar metallicity regimes (different by less than a factor of three over 7 Gyr). A factor of three difference in Z may exist between the extremes of the outer–Galaxy and the metal–rich galactic–centre populations.

Appendix B Turn-off from the AGB–evolutionary track

In this appendix, we discuss a method to determine upper age limits for an ensemble of OH/IR stars from their “turn–over” [25]–[60] colours in the IRAS two–colour diagram.

According to Garcia Lario (1991), OH/IR stars evolve along the evolutionary track (van der Veen & Habing 1988) in the IRAS two–colour diagram (Fig.B1) until they reach maximum colours (R_{32}^f, R_{21}^f) dependent upon their main–sequence mass. At that point, they leave the evolutionary track to evolve with approximately constant $R_{32} \equiv R_{32}^f$ toward higher R_{21} . The higher R_{32}^f , the higher the initial mass of a star :

$$\log M_i = \left(\frac{R_{32}^f + 2.42}{0.72} - 2.45 \right) / 3.2. \quad (\text{B1})$$

From Fig.B1 it is seen how one can thus determine the upper and lower limit to the initial masses and ages in a sample. The largest turn–over colour R_{32}^f is indicated by B and the smallest by A. With equation (B1) we find the highest and lowest masses present in the sample and with the isochrones by Bertelli et al. (1994) we find the corresponding lowest and highest ages. The lowest age thus found is an upper limit to the true lowest age as there may be younger stars that have not yet turned away from the evolutionary track (Fig.B1).

This paper has been produced using the Royal Astronomical Society/Blackwell Science T_EX macros.

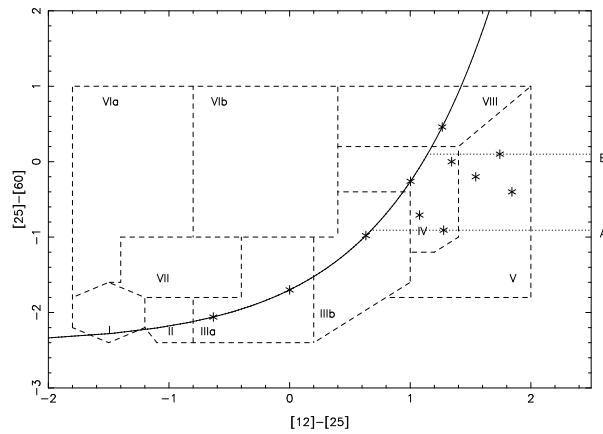


Figure B1 The IRAS two-colour diagram (van der Veen & Habing 1988). The colour R_{21} equals $[12]-[25]$ which is defined as $2.5 \log S_{25\mu\text{m}}/S_{12\mu\text{m}}$ and accordingly $R_{32} \equiv [25]-[60]$. The solid curve indicates the OH/IR-star evolutionary track; the dashed lines outline the various regions as they were defined by van der Veen & Habing (1988). The two dotted lines give the largest and smallest R_{32}^f (see text) for this fake sample.